Wetting behavior of olivine;
a 2D and 3D analysis of melt pocket geometries

Stan F. Aben*

Supervisors: Prof. Dr. M.R. Drury* and D.A.M. de Winter[+]

**Earth Sciences, Faculty of Geosciences, Utrecht University, The Netherlands*

[+]Electron Microscopy and Structural Analysis, Cellular Architecture and Dynamics, Faculty of Sciences, Utrecht University, The Netherlands

Key words: dihedral angle, olivine, stereology, tomography, focused ion beam, scanning electron microscopy

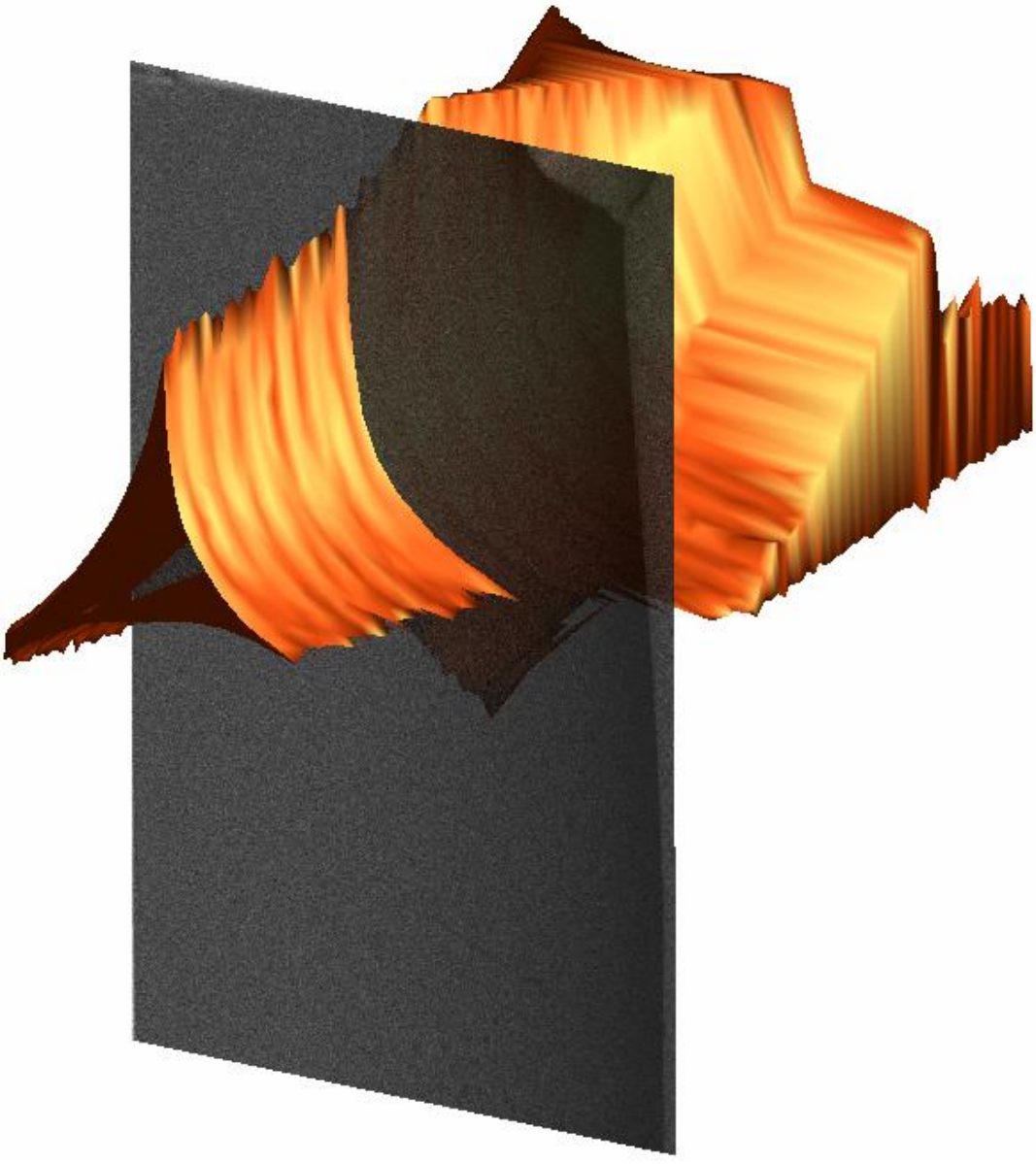

Content

Abstract

The characteristics of the distribution of melt through peridotites can strongly influence melt migration, as well as properties like seismic attenuation and mechanical strength, which are of major importance in many geological studies of the Earth's mantle. Melt distribution can be characterized by the wetting angle or dihedral angle, which quantifies the amount of protrusion of melt between individual melt pockets. Conventional studies of dihedral angles rely on the estimation of 3D dihedral angles from the distribution of 2D apparent angles. However, there are few studies on the relationship between the true dihedral angle and apparent angle distributions. Dihedral angle analyses have been performed on samples containing 95% forsterite (Mg_2SiO_4) and 5% enstatite ($MgSiO_3$) to gain more insight of the dihedral angle in olivine, which is a major constituent of the Earth's mantle. Imaged cross sections through true dihedral angles in different orientations result in images containing apparent dihedral angles in conventional data sets. To investigate the validity of different statistical approaches of the true dihedral angle, as well as the effects of faceting and melt content on the dihedral angle, a new method has been developed for both true dihedral angle and apparent dihedral angle analysis compatible with FIB-SEM imaging. Usage of the new method aims to reduce errors caused by magnification and resolution limitations as well as influences of arbitrary elements present in conventional methods. Accuracy is increased to up to 1-2° for apparent dihedral angles and ~3° for true dihedral angles. An arbitrary set of cross sections was created for the analysis of apparent angles. The dihedral angle estimated from the mean of these apparent angles is in good agreement with the true dihedral angle measured in the FIB-SEM datasets. Distributions of apparent angles suggest that faceting and the presence of zero-degree dihedral angles between grains have a major influence on dihedral angle distributions and with that, on statistical approaches of the dihedral angle. This could have implications in multiple fields of study on the Earth's mantle.

1. Introduction

1.1 Wetting behavior of olivine rock

Peridotites are one of the most abundant rock types in the Earth's mantle, and one of the key sources for information about the composition of the Earth (W.F. McDonough & S.-s. Sun, 1994). The pressure and temperature conditions in the mantle are often such that these olivine- and pyroxene-rich rocks exhibit complete or partial melting. The presence and nature of melt pockets, and possibly melt layers (Cmíral *et al*., 1998; R. De Kloe *et al*., 2000), could have major implications for the properties of the rock. For example, simple-shaped, well-connected intergranular spaces increases melt migration. Also, seismic attenuation increases with increasing melt abundance between grains and the mechanical strength of a rock is lowered by wetting of the grains (Schmeling, 1985; Hirth &

Kohlstedt, 1995; Cmíral *et al*., 1998), which influences the rocks rheology. The presence of the melt layers could be attributed to the increased melt content or to the increase in wetting with the associated decrease in contiguity (Hier-Majumder & Abbott, 2010). Olivine is the major constituent of ultramafic peridotites. Hence, in order to understand the behavior of peridotites in the Earth's crust and mantle, it is important to characterize and understand the behavior of olivine at pressure-temperature ranges typical for the Earth's crust and mantle. For example, olivine rheology is an important factor in glacial isostatic adjustment (GAI) studies. Isostatic rebound due to retreat of glaciers is associated with (variations in) mantle flow and therefore with the rheology of olivine (W. van der Wal *et al*., 2013).

The evolution of melt pockets in olivine is a gradual process, resulting in melt pockets with a great variety in geometries. (Cmíral *et al*., 1998). The geometry of a melt pocket is determined by multiple factors e.g. the crystal shape of the solid, the differences in pressure between the different phases, the presence of different minerals (e.g. pyroxene (Toramaru and Fujii, 1986)), and the wetting behavior (Hiraga *et al*., 2001). The latter can be investigated by studying the wetting angle or dihedral angle of the system. The dihedral angle represents the amount of penetration of melt along grain boundaries. The permeability of the system will increase as the dihedral angle decreases towards zero (Cmíral, 1998; Yoshino *et al*., 2009). The increase in permeability is related to a decrease in grain boundary contiguity. As a result, the dihedral angle is employed as a measure for the permeability and possible melt migration within the system. The term wetting angle is based on the fact that when the protrusion of the melt in between grain boundaries progresses, a larger amount of the grains becomes "wetted" as it comes into contact with the melt instead of an adjacent grain. Wetting angles could act as a source of information about cooling rates, solidification rates and textural evolution (Holness *et al., 2005),* as well as the thermal history of mafic rocks in the sub-solidus (Holness *et al*., 2012).

1.2 Dihedral angle

1.2.1 Surface free energy

The dihedral angle is mainly controlled by the shape of crystal surfaces, which in turn is controlled by a selection of transport mechanisms, like diffusion and condensation, and chemical reaction rates (Herring, 1951). When the dimensions of the crystal grains are large relative to the irregularities on the crystal surface, lowering of crystal surface free energy is the most important driving factor for changes in the surface structure of the crystal (Herring, 1951). The surface free energy is determined by the excess free energy of atoms at interfaces between phases (grain and melt) and at grain

boundaries. This free energy is per unit of surface area and is also dependant on temperature, pressure and the surface normal, which represents the direction of forces. In the case of isotropic crystals, in which the surface tension is equal to the surface free energy, the following equation gives the surface free energy:

$$\gamma = \left(\frac{\partial G}{\partial A} \right)_{T,P,n} \tag{1.1}$$

In which γ is the surface free energy or the surface tension, G is the Gibbs free energy and A is the surface area. Thermodynamics require that all spontaneous changes of state are accompanied by a decrease in the Gibbs free energy, which has consequences for the shape of the surfaces. Since surface energy is quantified by the breaking of intermolecular bonds when cleaving a solid, the presence of a surface is related to an excessive energy configuration. Creating a surface costs energy and is less favorable than the bulk. If the bulk would be energetically less favorable than a surface, there would be a driving force for the formation of a crystal surface and the crystal bulk would automatically be removed. As a result, grains will shrink, maximizing their surface area and minimizing their bulk volume. However, such is not the case and it is only the shortage of material that prevents crystals from continuous growth, resulting in crystal surfaces, even though energetically unfavorable. The surface free energy is the work needed to create a unit of surface area, independent of the temperature and the chemical potential. To minimize the amount of work the system will have a tendency towards minimization of surface area just like a drop of water minimizes its free surface energy by assuming a spherical shape. Although the system will have the tendency to have the lowest amount of energy for its surface, metastable equilibrium could be achieved in which the surface free energy is not at its minimum. In cases where surface diffusion is the main transport mechanism, metastable equilibriums can exist (Carter *et al,* 1995).

The surface free energy is always associated with the energy configuration at interfaces between phases and at grain boundaries. The drive to lower the surface free energy is reflected in the evolution of the dihedral angles, controlling the redistribution of liquid or melt throughout the volume into lower energy configurations (Cmíral *et al.,* 1998) Migration of melt is effectively caused by the stability of the energy configurations of a solid-solid interface (grain boundary) and the two solid-liquid interfaces between the melt pockets and each of the grains. (Smith, 1964; Cmíral *et al., 1998*) A more stable energy configuration at the solid-liquid interfaces would eventually lead to the disappearance of the grain boundary and complete wetting of the grains (Cmíral *et al; 1998*) and a

dihedral angle of 0°. The dihedral angle Θ, which form at junction points between the solid-liquid interfaces and the grain boundary is controlled by the balance in energy. Generally, a smaller dihedral angle leads to further transportation of melt in between grains. An example of a triple junction is shown in figure 1a. The grain boundaries are only partially wetted. The dihedral angle can be measured for all three grain boundaries. Figure 1b presumably shows complete wetting, as two neighboring grains have separated completely, with melt present between the grains. However, it should be noted that a two-dimensional image can be misleading, as figure 1b might show a triple junction (Figure 1a) cut along the long axis of a melt tube (Wark *et al.,* 2003).

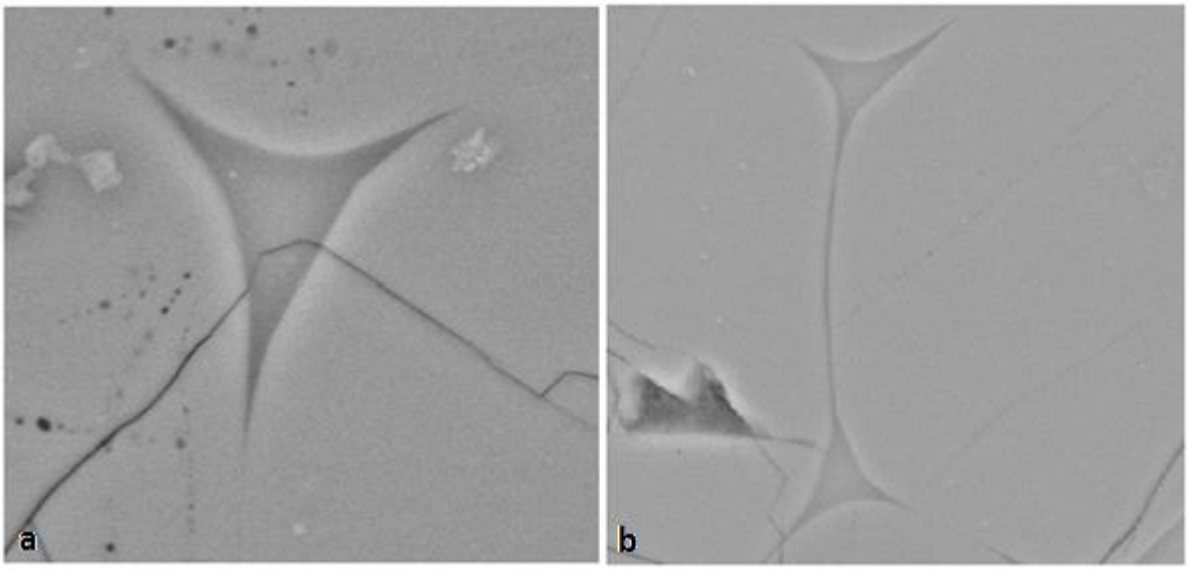

Figure 1.a. A triple junction with grain boundaries, touching in every direction. **b**. A microstructure showing separated grain boundaries. The apparent separation of the grain boundaries might be caused by the orientation of the cross section, cutting the microstructure along the long axis of a melt tube (Wark *et al.*, 2003). The black line is a crack in the sample and has no influence on the microstructure.

An increase in transport distance of the melt from multiple directions will lead to higher melt connectivity in the material and increased permeability. Materials with large dihedral angles, associated with a more stable energy configuration at grain boundaries rather than at the solid-liquid interfaces, will generally have more isolated melt pockets. The dihedral connects the energies of the grain boundary and the solid-liquid interface (Smith, 1964):

$$\cos\left(\frac{\Theta}{2}\right) = \left(\frac{\gamma_{gb}}{2\gamma_{sl}}\right) \tag{1.2}$$

Where γ_{gb} is the grain boundary surface free energy and γ_{sl} is the solid-liquid interfacial energy.

1.2.2. Anisotropy

In isotropic materials, surface free energy is equivalent to the surface tension of the system and no internal forces affect the energy balance at the surface. As a result, the equilibrium shape of a crystal is a sphere. The absence of heterogeneity in the material that would affect the surface free energy allows the surface free energies at both solid-liquid interfaces to be treated as equal. However, anisotropy in the surface energy of olivine is frequently encountered (Cmíral *et al;* 1998), as it is for most crystalline solids. When the solid is anisotropic, several additional factors play a role affecting the surface free energy. Apart from a dependence on temperature, chemical potential, or composition of the phases, also the relative orientation of the crystals affects the energy balance in the system (Cahn & Handwerker; 1993). The offset in orientation of the grains requires a modification of equation 1.2, taking into account two different surface free energy values of the solid-liquid interfaces.

$$\cos\left(\frac{\Theta}{2}\right)=\left(\frac{\gamma_{gb}}{\gamma_{sl}^{I}+\gamma_{sl}^{II}}\right) \tag{1.3}$$

Note that the relative orientation effects of the two neighboring grains are implicitly taken into account in γ_{gb}, which can be considered as a function of the surface normal and a rotation matrix representing the misorientation between both grains, as well as the pressure and temperature (Cmíral *et al;* 1998).

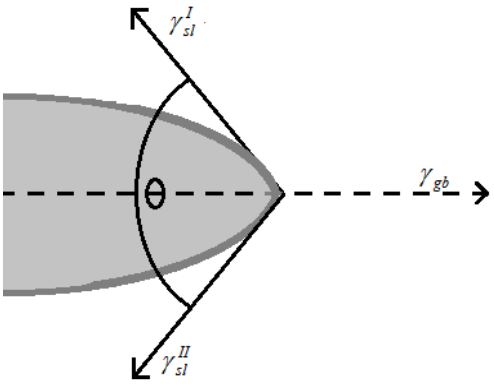

Figure 2. A representation of the interfaces that together determine the dihedral angle. The grain boundary surface free energy is represented by γ_{gb} and the solid-liquid interfacial energy is represented by γ_{sl}. The dihedral angle between two grains is represented by Θ. The liquid phase in the system is marked in grey.

1.2.3. Shapes of interfaces

In isotropic materials the shape of the solid-liquid interface is characterized by a mean curvature, which is directly proportional to the pressure difference at the interface. The pressure difference results in a force acting normal to the plane of the interface. If no pressure difference exists, no normal force will be present and the interface would be flat. The pressure difference between the mineral grains and the adjacent melt results in a curved solid-liquid interface. The tensile forces of the solid-liquid interface act in the opposite direction of the pressure, cancelling the tensile forces creating equilibrium. These forces are balanced following the Young-Laplace equation:

$$\Delta p = \gamma\left(\frac{1}{R_x}+\frac{1}{R_y}\right) \tag{1.4}$$

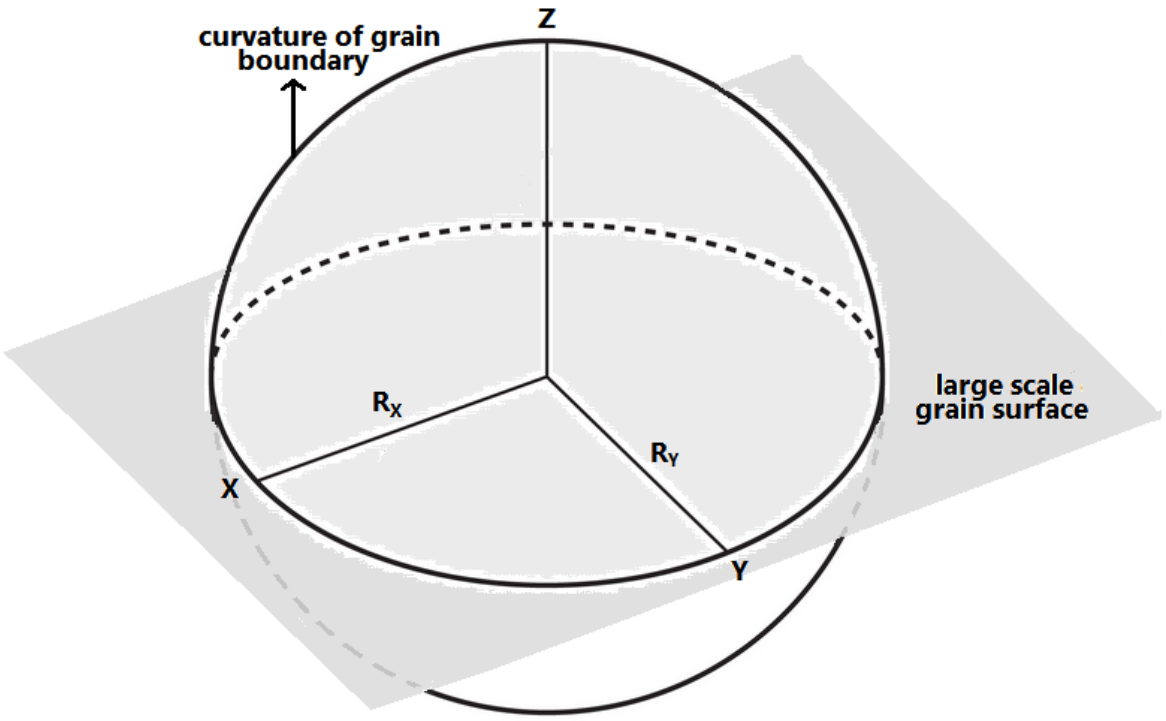

Figure 3. The large scale orientation of the grain surface is represented by the grey plane. On a smaller scale the geometry of the solid-liquid interface is represented by the upper part of the sphere. The radii of curvature Rx and Ry both lay on the axes that are parallel to the large scale orientation of the grain surface.

In which Δp = the pressure difference, γ = the surface tension and R_x and R_y are the radii of curvature in each of the axes that are parallel to the surface (figure 3). The shape of an anisotropic crystal is determined by the surface free energies of each of the crystal faces. Most significant in olivine is the relation between the surface free energy and the crystal orientation. Low Miller-indices crystal

surfaces have a lower interfacial energy configuration (Yoshino *et al.,* 2006), resulting in crystallographic-controlled grain growth, which is no longer related to wetting. Due to the anisotropic nature of olivine, an equilibrium shape may contain planar faces and sharp corners or rounded surfaces, depending on the amount of anisotropy in the crystal. The differences in the relative surface energies and the resulting corners create faceted solid-liquid interfaces called F-faces. The presence of F-faces is thought to have a major contribution in the overall melt distribution as the presence of flat interfaces effectively increases the cross sectional area of the midpoint of a melt triple junction. This is related to the lack of curvature in at least one of the interfaces. As a result the permeability of the system increases (Waff & Faul; 1992).

1.3 *Extracting the dihedral angle*

The measurement of dihedral angles has been the subject of many studies that either focus on the actual measurement of the dihedral angles (e.g. de Hoff, 1986; Felberbaum *et al*., 2004; Holness, 2006), statistical methods to extract the true angle (e.g. Harker & Parker, 1945; Jurewicz & Jurewicz, 1986; Gokhale & Zhang; 2013) and the use of dihedral angles in a geological framework (e.g. Cmíral *et al*. 1998; Hiraga *et al*., 2001; Holness *et al*., 2012). Direct measurements of the true dihedral angle are performed using a universal stage, which allows rotation and tilting of a sample under an optic microscope. Optic microscopy however, has limitations with regard to magnification, which limits the application of this technique. In most cases a cross section of the material of interest is made mechanically and from the images of the two-dimensional slices the dihedral angles are directly measured. Imaging of melt structures in olivine-basalt system is in most cases done by use of SEM (Wark *et al.,* 2003) and TEM (Cmíral *et al.,* 1998). The fact that the melt pockets are actually three-dimensional objects, poses complications for interpretation of the measured dihedral angle. A triple junction cut in an arbitrary plane will not show the real or 'true' dihedral angle. Therefore, statistical methods have been developed to approach the true dihedral angle, based on large numbers of measurements from two-dimensional sections.

The statistical approach was first introduced by Harker and Parker (1945) and later revisited by Jurewicz & Jurewicz (1986). Harker and Parker suggested that the median of an apparent angle distribution approaches the true dihedral angle with an accuracy of no more than one degree. Assumed was that there is only one unique dihedral angle present in the system. The presence of a variety of true dihedral angles with an unknown distribution was suggested by Stickles and Hucke (1964). The median dihedral angle was therefore considered to yield no specific information. A good match between a random dataset of apparent angles and the presence of a normal distribution of true dihedral angles around the median of the apparent angles was observed by Jurewicz and

Jurewicz (1986), suggesting that the median of apparent angles is a good representation of the true dihedral angle. Gokhale & Zhang (2013) also suggested a new stereological relationship for estimating the mean value of the sine of the dihedral angles from the measurements of apparent section angles that are isotropic, uniform and random (IUR). The success of such statistical techniques however, is only guaranteed provided that the sampling is IUR (Goodwin *et al*.; 2009).

1.3.1 "Gokhale and Zhang" equation

The mean value of the population apparent angles $<\Psi>$ observed in IUR 2D planes is equal to $<\chi>$ which is the mean value of distribution of true dihedral angles, yielding equation (1.5). The characterization of the distribution of true dihedral angles requires the mean value of true dihedral angles and a measure of the spread. Gokhale and Zhang (2013) presented a new general stereological relationship for the estimation of the mean value of the sine of the dihedral angles in a true dihedral angle distribution (equation 1.6). This determination can be performed based on measurements of apparent angles in IUR 2D sections. The mean and the variance of a true dihedral angle distribution that could be represented by a two-parameter distribution function can be calculated using these two equations.

$$\langle \chi \rangle = \langle \Psi \rangle \tag{1.5}$$

$$\langle \sin X \rangle = (1/\pi)\left\langle \left[\Psi(\pi - \Psi) + \sin^2 \Psi \right] \right\rangle \tag{1.6}$$

1.3.2. Ambiguity of dihedral angle measurements

Regardless of statistical analysis techniques used to estimate the true dihedral angle, conventional measurements are sensitive to error. A restriction of conventional SEM and TEM imaging is that the quality of the imaging decreases with increasing magnification. At very high magnifications, the detail that is necessary for accurate dihedral angle measurements could become indistinguishable. The outcome of a manual measurement of the dihedral angle will not only be dependent on the precision of the analyst, but in a higher degree also on the ability to distinguish the point at which the solid-liquid interface becomes a solid-solid interface. Higher magnifications in this case lead to a higher precision emplacement of this point and therefore in more accurate measurements of the dihedral angle.

Conflicting suggestions in the field of statistical analysis of 2D dihedral angle data call for a validity check of the statistics used for this purpose. True dihedral angle data is necessary to achieve this. Analysis of the true dihedral angle by use of a universal stage and optical microscope cannot be performed in some cases due to the limitations in resolution of optic microscopy, while direct measurements of the true dihedral angle by TEM are highly arbitrary. A less arbitrary method for 3D true dihedral angle analysis, compatible for high resolution SEM imaging is therefore desired. Influences of other erroneous factors like magnification, limited resolution and biased and arbitrary measuring should be decreased as well. The aim of this study is to develop a method, which is able to produce a reliable data set that could provide more insight in the validity of several statistical methods. The produced data can also be used to increase knowledge about the influence of phenomenon like faceting and melt layers on dihedral angles.

2. Materials and Methods

2.1. Samples

The present study makes use of a set of synthetic polycrystalline forsterite samples, previously used by De Winter *et al. (2008)* and Ten Grotenhuis *et al. (2004)*. The samples are 10 mm in diameter and approximately 1-1.5 mm thick. The samples are composed of a combination of forsterite and enstatite, which are the magnesium-rich end members of the olivine and pyroxene mineral groups. The composition of the starting material is 95% forsterite (Mg_2SiO_4) and 5% enstatite ($MgSiO_3$). The average grain size of the material is 1.1 +/- 0.4 µm. Two samples have been sintered for 240 minutes and two samples have been sintered for 180 minutes. A melt/glass has been added to the samples, which is composed of 29% MgO, 20% Al_2O_3 and 51% SiO_2. The melt contents are 2.5%, 3.5%, 5% and 10% respectively. An overview of the used samples is given in table 1. All phases present in the sample are insulators and are susceptible to electrical charging during conventional electron imaging. In order to reduce charging, the samples were coated with carbon, gold or platinum. See Ten Grotenhuis *et al.* (2004) for further detail.

Melt content (%)	**Sinter time (min)**	**Final grain size (µm)**
10%	180	25,7
5%	180	ND[a]
3,5%	240	39,5
2,5%	240	ND[a]

Table 1. [a] ND is not determined.

2.2 *SEM imaging*

A Scanning Electron Microscope (SEM) (XL30, FEI, Eindhoven, The Netherlands) was used for imaging large numbers of dihedral angles from cross sections. Images are recorded with electron beam acceleration voltages between 10kV and 15 kV. Contrast between the grains and melt structures is found using the ETD (Everhart Thornley Detector) in BSE mode. In addition CL (Cathodeluminescence) imaging will be done to obtain information about present minerals and possibly chemical zoning in minerals. Magnifications range from approximately 1000x to 18000x.

2.3. FIB-SEM imaging

Data for 3D analysis purposes was collected using a Focused Ion Beam – Scanning Electron Microscope (Nova Nanolab 600 Dualbeam, FEI, Eindhoven, The Netherlands). The FIB focuses Ga^+ ions onto the surface. Momentum transfer from the ions sputters away atoms from the sample, a process called milling (Volkert & Minor, 2007). As a result, trenches in olivine can be milled in the

range of nanometers to tens of micrometers. A well-known application is called FIB-SEM tomography (Uchic *et al.*, 2006; De Winter *et al.,* 2008), or Slice & View^{tm} (FEI, Eindhoven, The Netherlands). The FIB mills consecutive cross sections, which are imaged by the SEM. The stack of SEM images is subsequently processed into a three-dimensional visualization of the structure. After finding a suitable area with the SEM, the area is protected by a roughly 1 µm thick layer of Pt deposition, which is deposited in-situ using the Gas Injection System (GIS). Subsequently trenches are milled around the area of interest and a final cross section at the front size. Before the final polishing step of the cross section, a fiducial marker is created left of the area of interest. The fiducial marker is used for automated alignment procedures of both the FIB prior to milling and the SEM prior to imaging. The FIB conditions are 30 kV, 0.3 nA, with a nominal slice thickness of 100 nm. SEM imaging conditions were 5 kV, immersion lens in BSE mode.

2.4. 2D data processing

2.4.1. Measuring the dihedral angle (2D)

To facilitate the measurements of dihedral angles, a software tool is developed (Delphi 5, Borland). The software allows manually indicating a number of points along both grain boundaries. From the coordinates, the software works out the point of intersection between both grain boundaries and the corresponding dihedral angle. The mathematical model behind the calculation assumes that (parts of) the grain boundaries can be approximated by circles. A short description of the model will be given in the next section. The complete description including the mathematics can be found in appendix A.

For the construction of the circles describing the curvature of the grain boundaries, both the centre point coordinates as well as the radius of the circles should be known. Three or more points are manually selected along each grain boundary. The normal of the lines connecting the points and cutting the connecting line in the middle, intersect at the circle's centre point coordinates. A spread of the coordinates is found when more than three points are used. Such spread could be the result from either incorrect selection of grain boundary coordinates or from the grain boundary deviating from a perfect circle. In case of a spread of coordinates for the circle centre, average coordinates are used. The radius of the circle is determined by averaging the distances between the centre point and each of the selected coordinates. The intersection point between the two circles represents the junction point. The tangents of both circles are the best representation of the "orientation" of the grain boundary in the junction point. To determine the intersection point, the equations of both circles (based on the known centre points and radii) are solved. The dihedral angle follows from the

tangents of both circles at the intersection point. In the case of a strongly faceted grain boundary, the geometry of the grain boundary can be approached by an infinitely large circle. However, practically it is much easier to define a straight line. In this case, the dihedral angle is represented by the angle between the tangent of the circle and the straight line in their intersection point. The mathematical description can be found in the second part of appendix A.

2.4.2. Extracting dihedral angle (3D)

Preparation of slice & view images

The inclination of the FIB cross section with respect to the SEM requires a post-processing step to correct for the projection view. The correction is performed by stretching the images in the y-direction by a factor $1/\cos(\alpha)$ where α is the angle between the detector and the imaged surface, which is 38 degrees.

2.4.3. IMOD modeling

The volume analyzed by FIB-SEM tomography is reconstructed using IMOD [Kremer et al., 1996]. The images are carefully aligned using IMOD tools (Etomo and Midas). Proper alignment of the slices is crucial to obtain reliable results for the dihedral angle. After the alignment the volume is segmented manually, resulting in the 3D reconstruction of the grain boundaries. Before viewing the result, the isotropy of the voxels must be corrected, as the slice thickness is much greater than the XY voxel size. The correction is performed by stretching of the model in Imod. The stretch factor used is depends on the slice thickness, and is proportionate to the scale of the images. The factor is determined by taking the length described by the scale bar in the image and dividing it by the amount of pixels in the scale bar. This gives a true length per pixel in the XY plane. To make the model proportionate in all directions , the amount of voxels present in a slice should be known. The voxels must have the same dimensions in each direction. The final step is dividing the true slice thickness by the true length per pixel to obtain the amount of voxels that fit in between two slices. The obtained amount represents the stretch factor. Once the proportionate volume is obtained, the model will be rotated to the desired rotation for analysis of the true dihedral angle.

3. Results

3.1. Software accuracy

The accuracy of and precision of the program were tested using an image of two constructed circles with a known angle. Average values were used to check the accuracy of the program. The dihedral angle between the two circles in the test image is 57,9° (Figure 4). A set of 20 measurements (table 2) was performed resulting in an average value of 58,63°. The accuracy of the program is thus 1-2°. The average deviation of the measurements is 1,2°. The standard error of the program can be determined from the standard deviation of the measurements, which is 1,66°. The circle or straight line approaching the grain boundary of the first grain as well as the lines used to determine its centre point are drawn in a light blue color. The manually picked coordinates for this grain, as well as the chords connecting the coordinates are drawn in green. The colors used for the second grain are yellow and dark blue respectively.

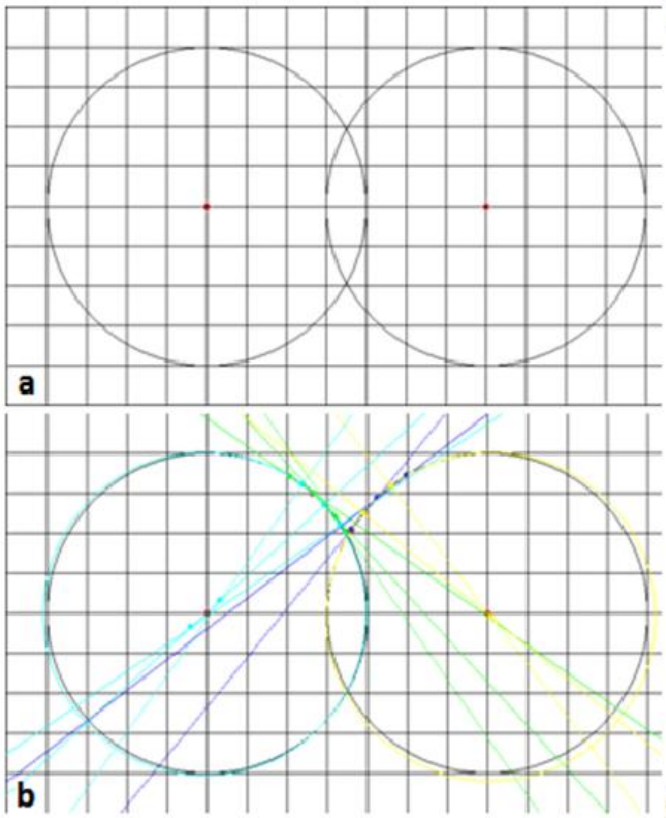

c

Measurement	Dihedral angle
1	58,14
2	62,28
3	61,24
4	55,32
5	57,03
6	60,31
7	61,28
8	60,47
9	59,69
10	58,7
11	56,23
12	56,96
13	57,5
14	58,58
15	58,39
16	61,69
17	54,78
18	58,32
19	57,68
20	58,04

Figure 4.a. Two circles were used to test the accuracy of the software. The “dihedral angle” between the two circles can be calculated mathematically. **b.** an example of a measurement of the known dihedral angle. **c.** All data collected during the accuracy check of the software. Overall, only small deviations from the known angle (57,9°) were observed.

3.2. Magnification test

The influence of magnification on results of dihedral angle measurements was tested by measuring the dihedral angle between two circle with known centers and radii. Measurements performed on the same dihedral angle at different magnifications resulted in different dihedral angle values. The blue measurers, used for a qualitative comparison of the measured dihedral angles, clearly show that a measurement at higher magnification results in a smaller dihedral angle (Figure 5a). Similar analyses were performed on a single dihedral angle in a real sample (Figure 5b). The determinations of the dihedral angle at several magnifications by means of visually approximating the tangents of the grain boundaries at the junction point showed results similar to those observed in the simplified model.

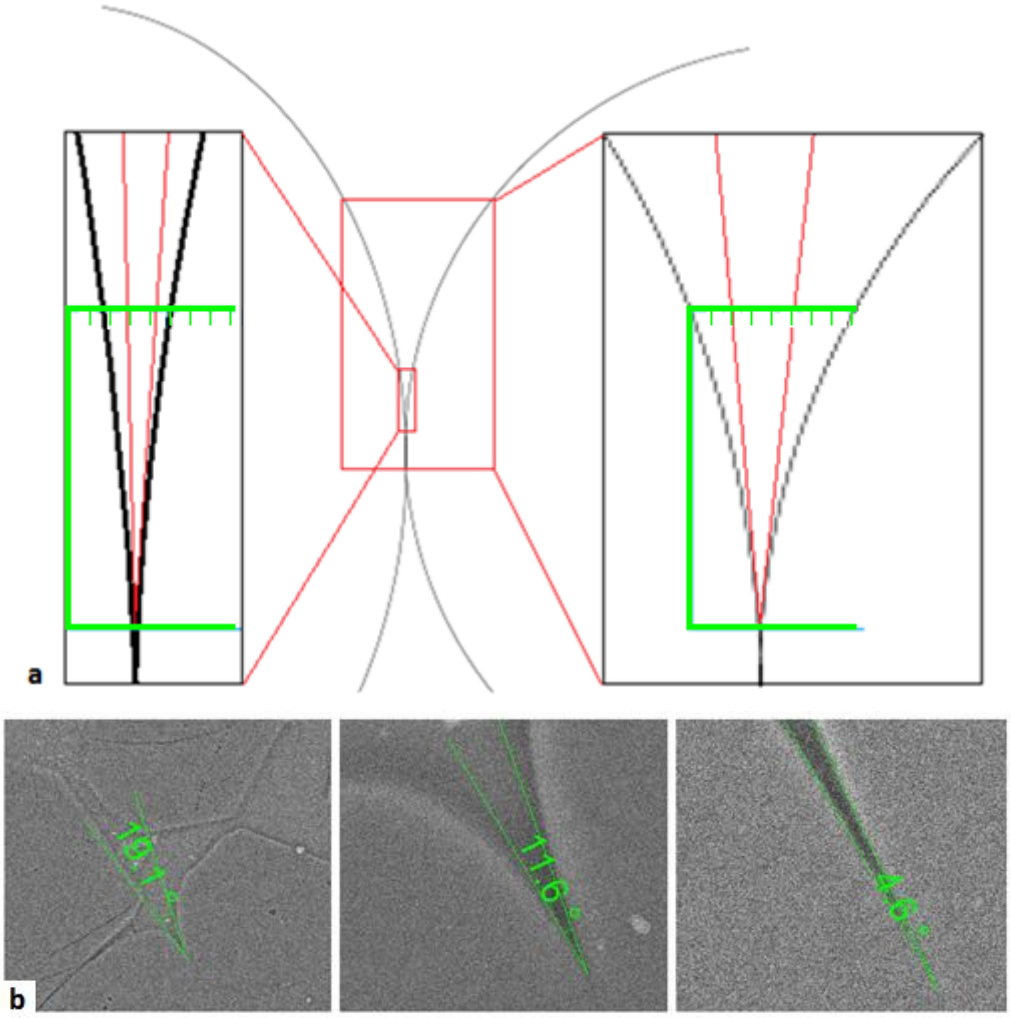

Figure 5.a. Visual approximation of the tangents of two circles, performed at different magnifications results in different values for the dihedral angle between the circles. The green measurers are exactly the same size. The approximation of the tangent is more accurate due to the availability of more detail regarding the junction point at higher magnifications. The resolution of the images should be sufficient to distinguish the detail as well. **b.** Measurements of the dihedral angle by visual approximation of tangents performed at different magnifications in a real sample give decreasing dihedral angles with increasing magnification.

3.3. Imaging

3.3.1. 2D imaging

Different magnifications were used for imaging of the samples, related to the dimensions of the microstructures present in each sample. The quality of the best possible images for each sample varies. The images of the F1 sample were taken at magnifications ranging from approximately 1000x to 8000x, with lower magnification images for an overview. Overall, the images show sufficient contrast for distinction between melt and solid. The resolution of the images is sufficient over the whole range of magnifications, allowing accurate analyses at the scale of the overviews as well as on the scale of the individual microstructures. Images for the E1 sample were taken at lower magnifications ranging from approximately 1000x to 4000x. Images of the E1 sample are of slightly lesser quality than the F1 images, but both contrast and resolution over the entire range of magnifications are sufficient. Images for the A3 and G1 were taking at the respective magnification ranges of approximately 1000x to 3000x and 5000x to 25000x. The A3 images are of similar quality as the F1 images. Although the quality of the images of the samples F1, E1 and A3 is good, the overall quality of the G1 sample images is relatively poor. The resolution of the samples is not optimal for the distinction of the grain boundary geometry of some microstructures. The general quality however, is sufficient for accurate analyses. Overall the quality of the images decreases with increasing magnification. Representative examples of images for each sample are given in appendix B.

3.3.2. CL imaging

FIB-SEM imaging using a CL detector was done to collect a dataset of representative CL images for all samples. In general images are all overviews of the samples. Samples with different melt contents showed different results. The 2,5% melt sample clearly showed a large number of dark grains as well as a smaller number of bright grains in CL. Melt could not be distinguished clearly in the 2,5% melt sample. However, images of the samples with higher melt content showed well-distinguishable melt between grains. Images of the 10% melt sample showed bright grains in sharp contrast with darker melt. Contrast in CL levels between melt and grains seems to decrease with decreasing melt content, as well as “flipping” towards darker grains with respect to brighter melt. The overall quality of the images is sufficient for analysis.

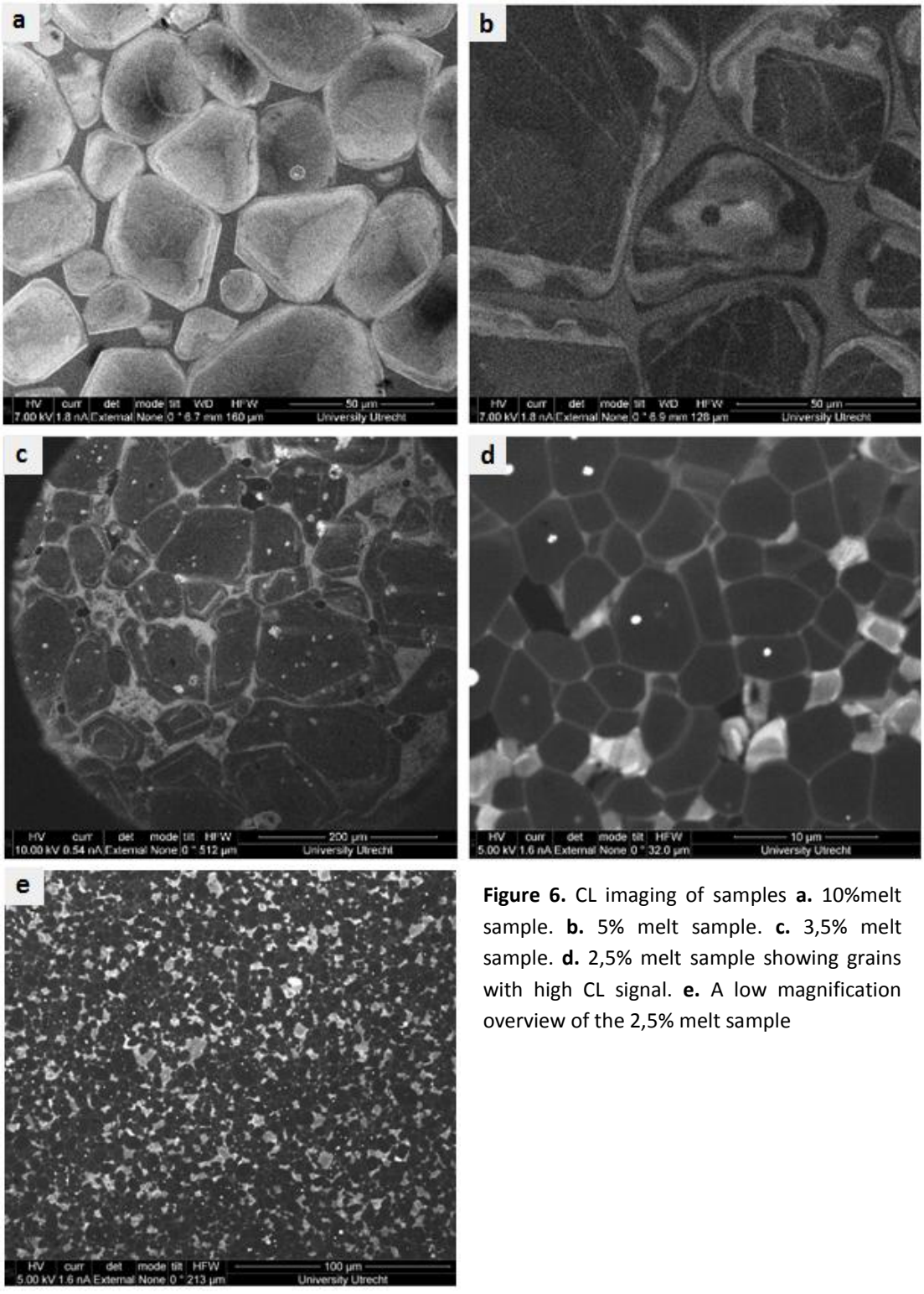

Figure 6. CL imaging of samples **a.** 10%melt sample. **b.** 5% melt sample. **c.** 3,5% melt sample. **d.** 2,5% melt sample showing grains with high CL signal. **e.** A low magnification overview of the 2,5% melt sample

3.4. Extracting dihedral angle

The software tool was used to load an image of choice after which coordinates along the grain boundaries in the pictures were selected. There is an option in the program to make a distinction between coordinates that correspond to a curved grain boundary and coordinates that correspond to a faceted grain boundary. We've used the software tool to measure the dihedral angles. The output of the program is an image containing the constructed circles and/or lines approaching the grain boundaries as well as the lines used to construct them, and a text file containing all coordinates and values for radii and dihedral angle. Two examples of output images are shown in figure 7. In order to make sure that the approach of the dihedral angle using this program is correctly performed, a visual check should follow after each coordinate selection and calculation to make sure that the constructed circles are good representations of the grain boundaries they should describe.

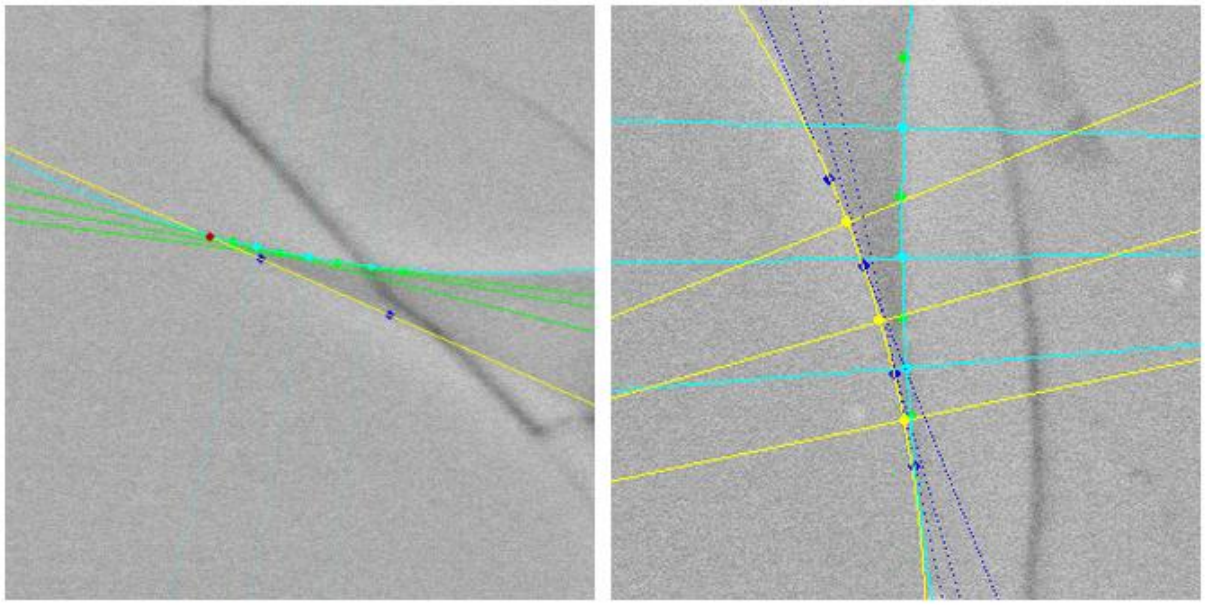

Figure 7. Output of the software tool; an image with the lines approaching the shape of the grain boundaries. On the left a faceted grain boundary is present. Analyses were performed on the F1 sample (10% melt).

3.5 2D data sets

A large amount of measurements was performed on the 2D images obtained by SEM imaging. An overview of all data collected in 2D is given in table 3. The complete datasets, containing all measured dihedral angles can be found in appendix B. Some examples of measurements can be seen in figure 8.

Melt content	*Analyses*[a]	*Angles*[a]	*0° angles*[a]	*mean*	*median*	*std. dev. all angles (range)*[b]	*Ave. std. dev.*[c]	*magnification*
10%	264	53	9	6,50	6,39	3,80	0,95	1000x – 8000x
5%	71	28	15	12,42	0	15,45	0,79	1000x – 4000x
3,5%	181	47	20	6,43	4,008	6,27	1,21	1000x – 3000x
2,5%	395	74	3	44,68	38,28	25,05	1,80	5000x – 25000x

Table 3. [a] the number in the table stands for the number of analyses, angles and 0° angles in the data. [b] The standard deviation of all measured angles from the mean dihedral angle of each sample. [c] The mean value of all standard deviations of separate angles in each sample.

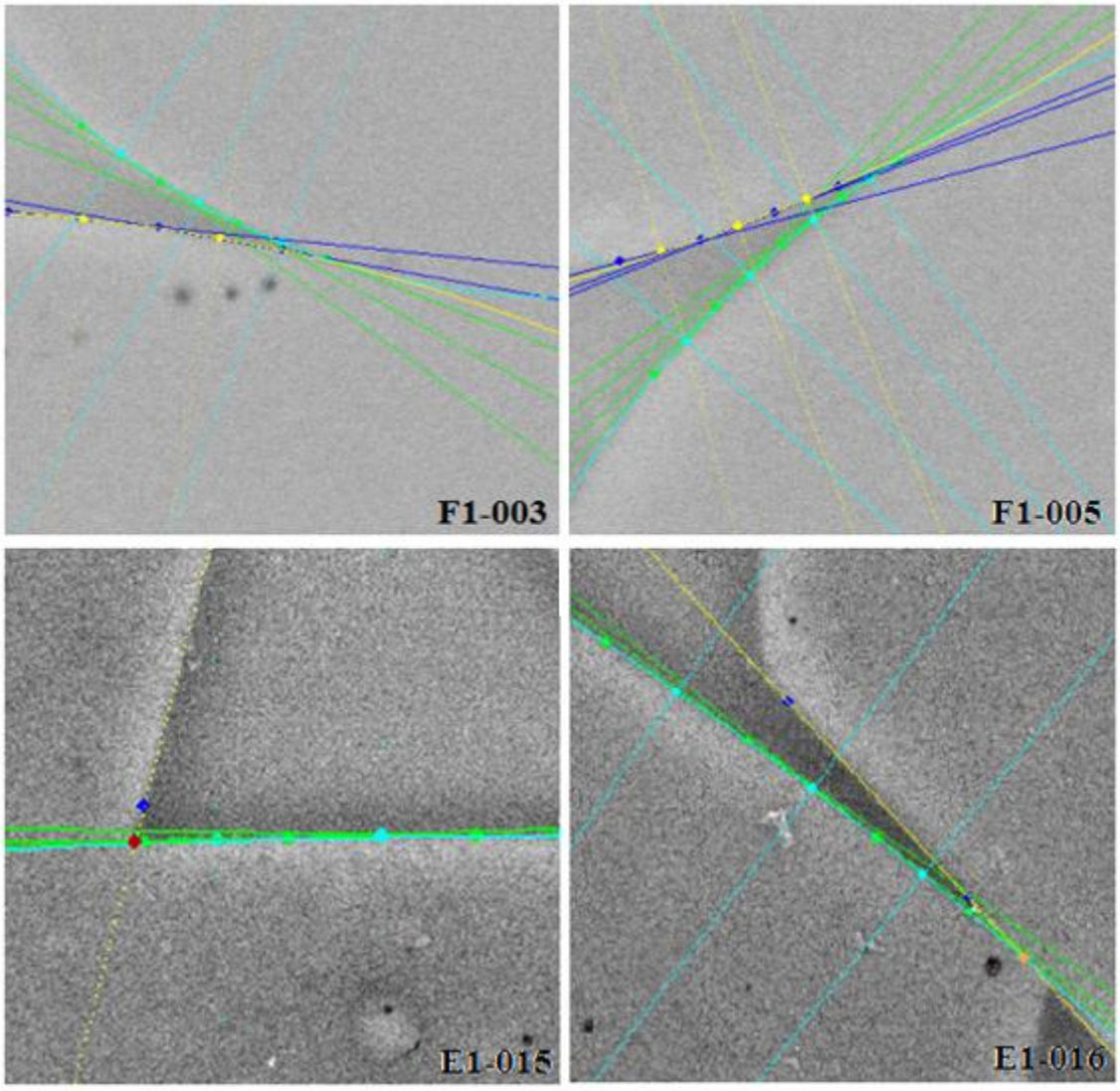

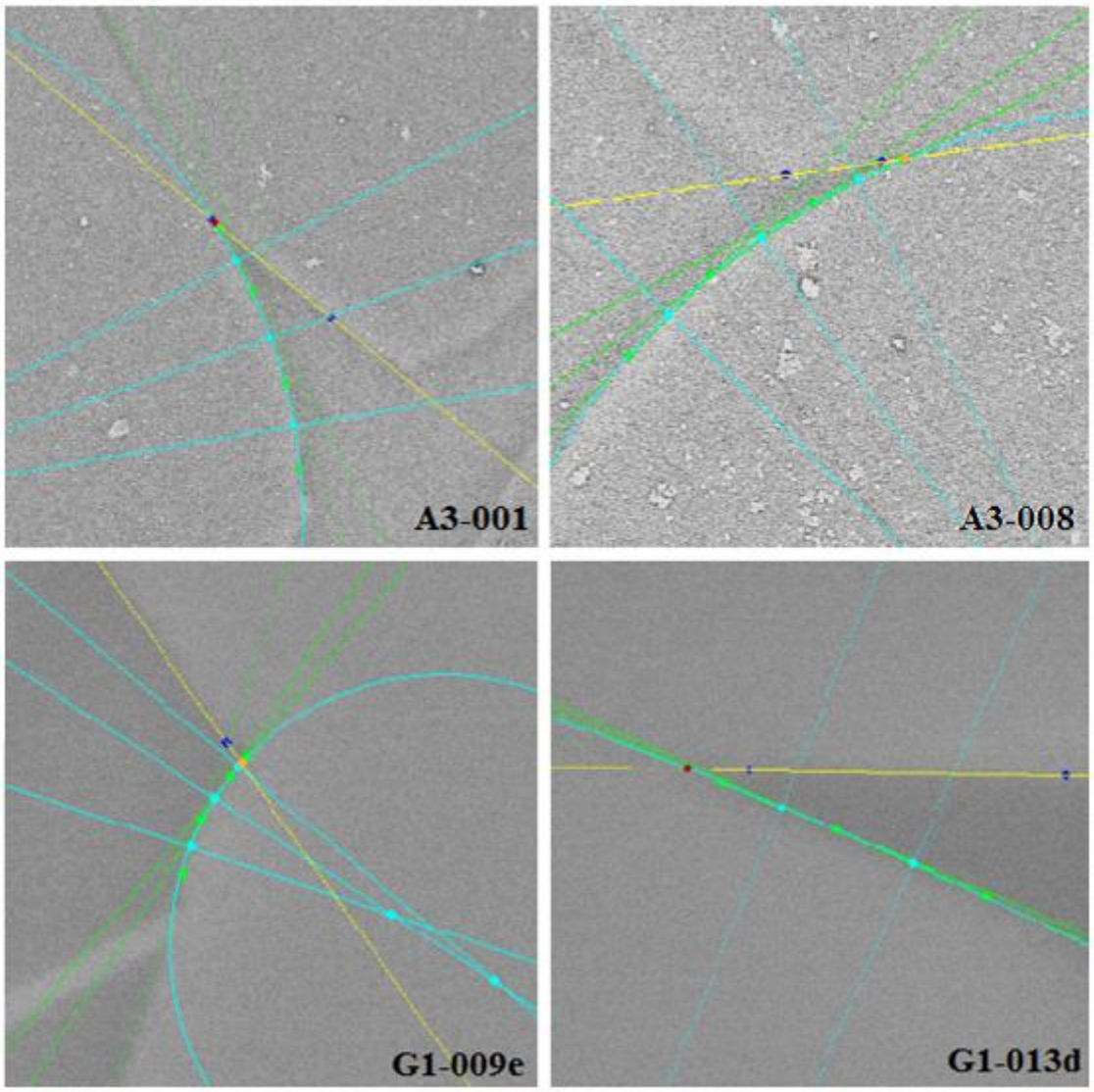

Figure 8. Example measurements of the dihedral angle in each sample. For each of the samples a measurement of a dihedral angle using two circles and a measurement using a straight line and a circle are shown. The first two signs of the codes in the bottom right corners of the images represent the sample box codes.

3.5.1 Faceting

Table 4 shows the proportions of the dihedral angles that were measured between grains without faceting and grains with faceting. Dihedral angles measured between two grains, from which only one grain is faceted were counted as faceted.

melt content	faceted	percentage[a]	non-faceted	percentage[a]	total angles[b]
10%	22	45 %	27	55 %	49
5%	12	67 %	6	33 %	18
3,5%	16	53 %	14	47 %	30
2,5%	52	72 %	20	28 %	72

Table 4. [a] The percentage of the previous column. [b] The total amount of dihedral angles taken into account.

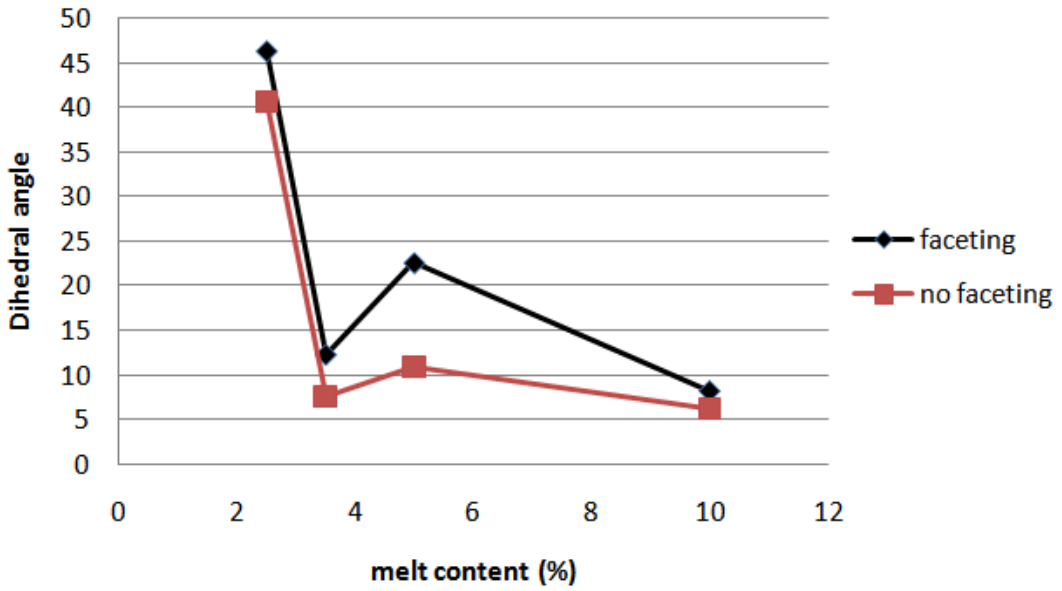

Figure 9. The influence of dihedral angles that are measured between faceted grains on the average dihedral angle is most significant in the 5% melt sample compared to the other samples. The other samples show a much smaller difference between the mean dihedral angle of faceted grains versus the mean dihedral angle of non-faceted grains.

Table 5 shows the mean and median dihedral angles for faceted angles and non faceted angles. The difference between the dihedral angles for each samples was expressed by a factor of increase from the non faceted dihedral angle to the faceted dihedral angle. Table 6 is shows the same data as table 2, but without the 0° dihedral angles. The 0° angles were not taken into account here.

melt content	mean faceted	median faceted	mean non-faceted	median non-faceted	f.o.i.[a] mean	f.o.i.[a] median
10%	8,23	7,93	6,27	6,39	1,31	1,24
5%	22,53	6,21	10,86	10,31	2,07	0,6
3,5%	12,29	9,54	7,54	8,27	1,63	1,15
2,5%	46,21	42,09	40,53	34,59	1,14	1,22

Table 5. [a] Factor of increase, which is the ratio of the mean and median dihedral angles of faceted dihedral angles **:** non-faceted dihedral angles.

melt content	mean faceted no 0°	median faceted no 0°	mean non-faceted no 0°	median non-faceted no 0°	f.o.i.[a] mean	f.o.i.[a] median
10%	9,06	8,44	7,06	6,87	1,28	1,23
5%	30,04	22,85	16,3	15,82	1,84	1,44
3,5%	13,1	9,75	8,8	9,2	1,49	1,06
2,5%	47,99	43,65	42,66	37,74	1,12	1,16

Table 6. [a] Factor of increase, which is the ratio of the mean and median dihedral angles of faceted dihedral angles **:** non-faceted dihedral angles.

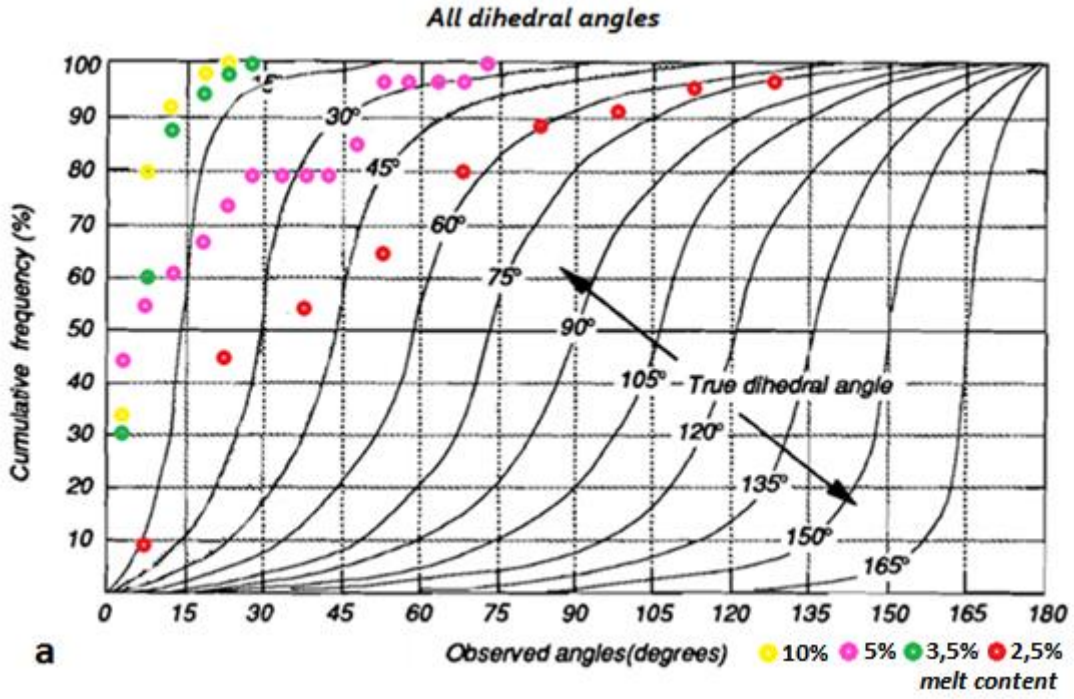
All dihedral angles
Cumulative frequency (%)
100
90
80
70
60
50
40
30
20
10
0
15
30
45
60
75
90
105
120
135
150
165
180
15°
30°
45°
60°
75°
90°
105°
120°
135°
150°
165°
True dihedral angle
Observed angles(degrees)
10%
5%
3,5%
2,5%
melt content

a

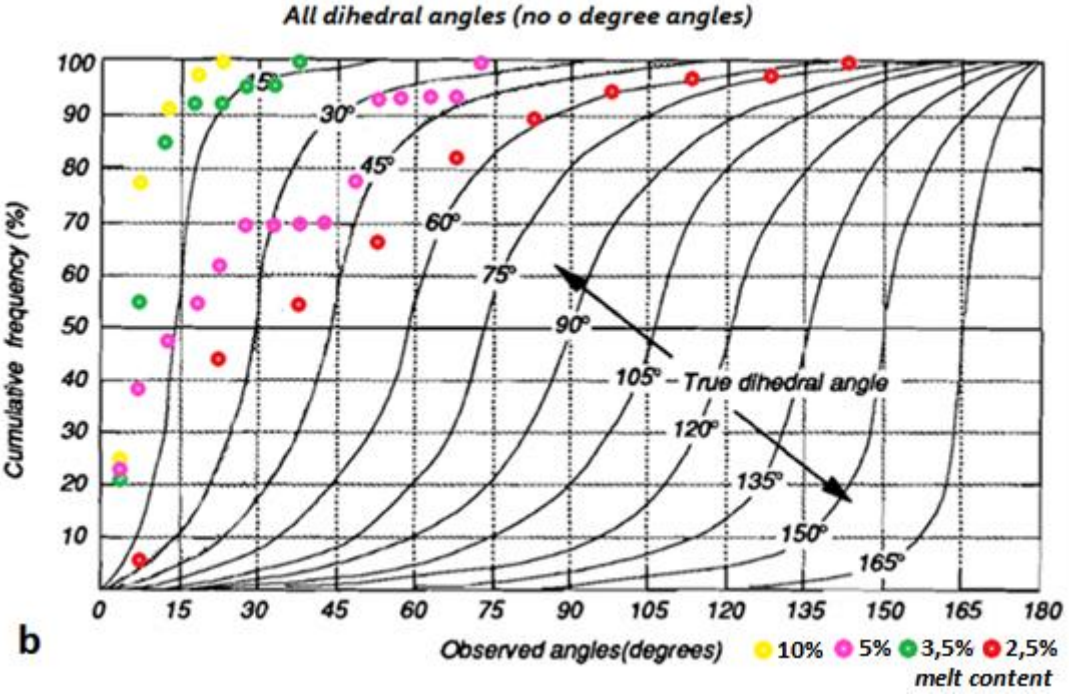
All dihedral angles (no o degree angles)
Cumulative frequency (%)
100
90
80
70
60
50
40
30
20
10
0
15
30
45
60
75
90
105
120
135
150
165
180
15°
30°
45°
60°
75°
90°
105°
120°
135°
150°
165°
True dihedral angle
Observed angles(degrees)
10%
5%
3,5%
2,5%
melt content

b

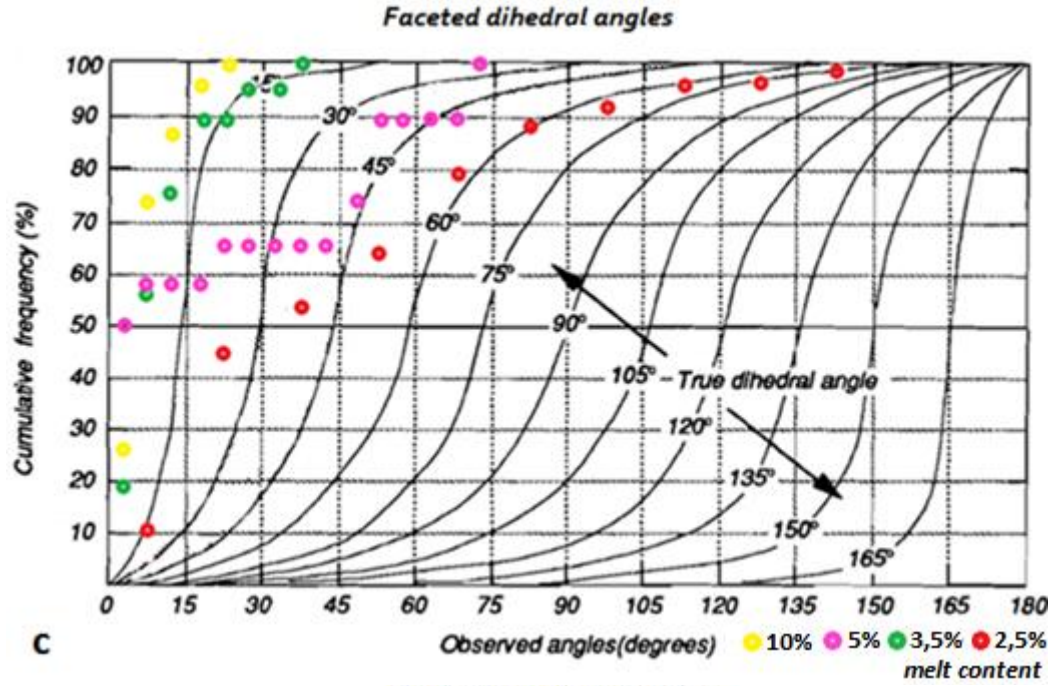
Faceted dihedral angles
Cumulative frequency (%)
15°
30°
45°
60°
75°
90°
105° – True dihedral angle
120°
135°
150°
165°
0 15 30 45 60 75 90 105 120 135 150 165 180
Observed angles(degrees)
10% 5% 3,5% 2,5%
melt content

c

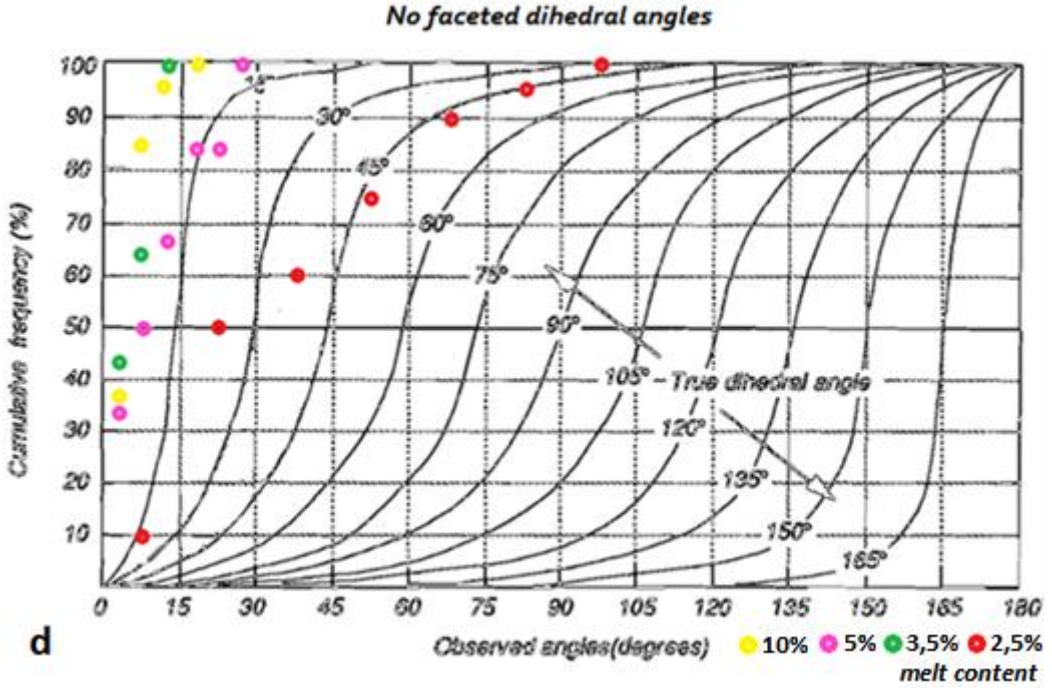
No faceted dihedral angles
Cumulative frequency (%)
15°
30°
45°
60°
75°
90°
105° – True dihedral angle
120°
135°
150°
165°
0 15 30 45 60 75 90 105 120 135 150 165 180
Observed angles(degrees)
10% 5% 3,5% 2,5%
melt content

d

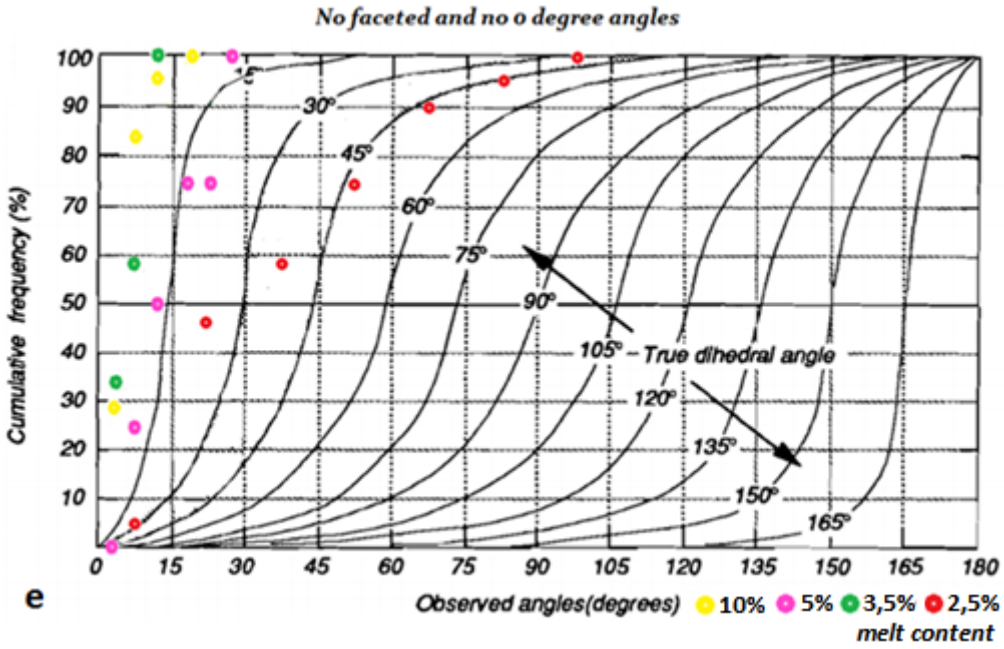

Figure 10. Cumulative frequency plots of **a.** all dihedral angles measured in the SEM images. **b.** only non-zero dihedral angles, including angles between faceted grains. **c.** only dihedral angles between faceted grains, including zero-degree dihedral angles. **d.** only dihedral angles between non-faceted grains, including zero-degree dihedral angles. **e.** only non-zero dihedral angles between non-faceted grains.

3.5.2. Radii of curvature

A plot of the radii of curvature versus the melt content was made. Only radii of curvature from grain boundaries at junction points with no fully developed faceting were taken into account. The graph shows no data for the 5% melt because of insufficient data for this sample. The overall trend in the graph shows an increasing mean radius of curvature with decreasing melt content. The range of observed radii of curvature increases with decreasing melt content as well.

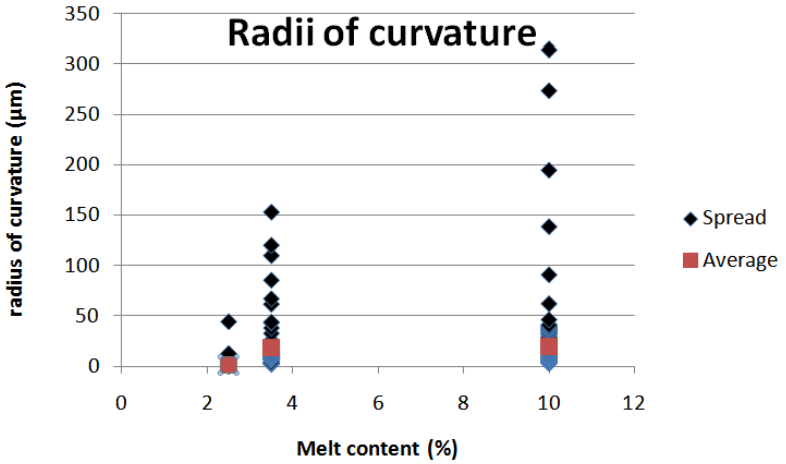

Figure 11. Plot of the radii of curvature versus melt content. The 5% melt sample is not represented in the plot due to lack of significant data. Overall an increase in mean radius of curvature as well as range of radii of curvature with increasing melt content can be observed.

3.6. 3D data set

The “Slice and View” method produced a set of images from consecutive slices of a block of the sample within an area of interest. The selection of the microstructure of interest in the separate slices, resulted in smooth 3D representation of the microstructure of interest (Figure 12). The modeled microstructure from the F1 sample (10% melt) that was used for the true dihedral angle measurements can be seen in figure 13a. The melt pocket can be seen from various different angles. Measurements were performed on constructed cross sections of this model. Faceting can be observed in the model as well (Figure 13b).

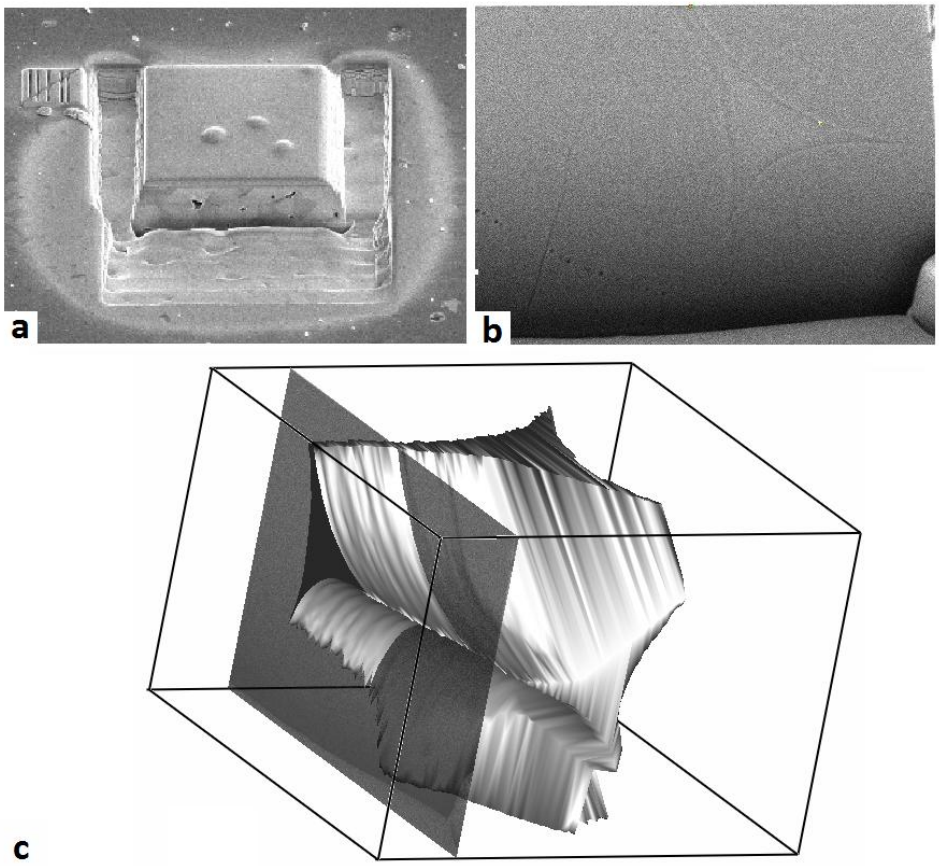

Figure 12.a. Image of the trenches milled with the FIB, resulting in a block suitable for “Slice and View” within the area of interest. **b.** A single slice of the block, containing a melt pocket. **c.** The orientation of the slice in the 3D model.

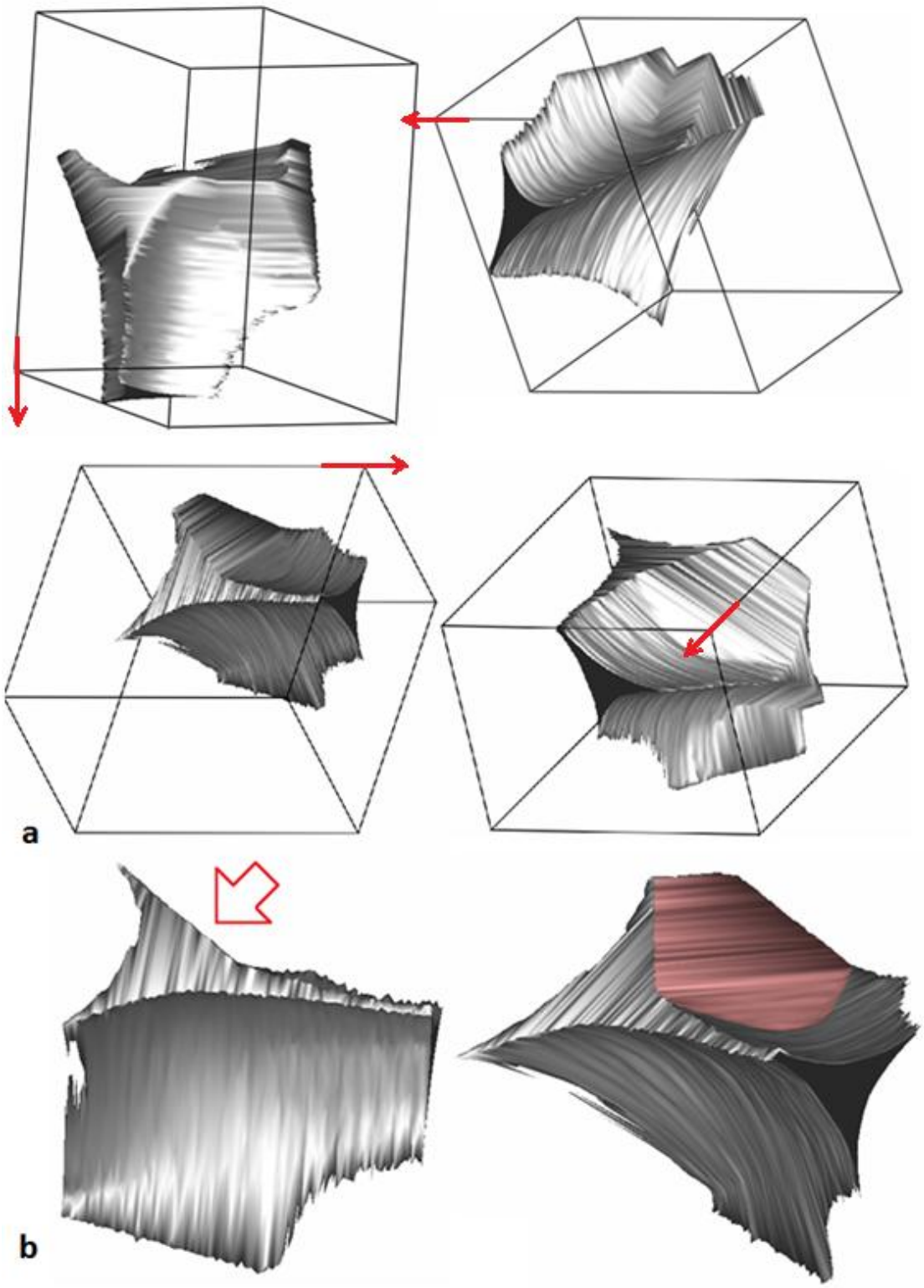

Figure 13.a. 3D model of the microstructure used for 3D analysis seen from different angles. The red arrows can be used as a reference regarding the orientation of the model. **b.** Faceting was observed in the 3D microstructure. An individual facet is shown from two directions. The arrow points at the facet in a side-view of the facet, which clearly shows the flat surface of the facet. The facet is marked in red in the adjacent image showing that the facet has a curved boundary due to the rounder shape of the adjacent part of the grain.

3.6.1. Data modification

The true dihedral angle can only be measured in one particular plane. In the three dimensional model, the normal of the plane of interest equals the direction vector. The direction vector is the vector connecting two points at equal distances along the z-axis on both sides of the point of interest. The points are the intersection points of the grain boundaries at the junction. The plane is chosen as such that its normal vector aligns with the previously described direction vector (Figure 14). This was done by determining the coordinates of the junction point in the positive and negative z-direction of the point in which the true dihedral angle should be measured, and taking the position vector of one point relative to the other.

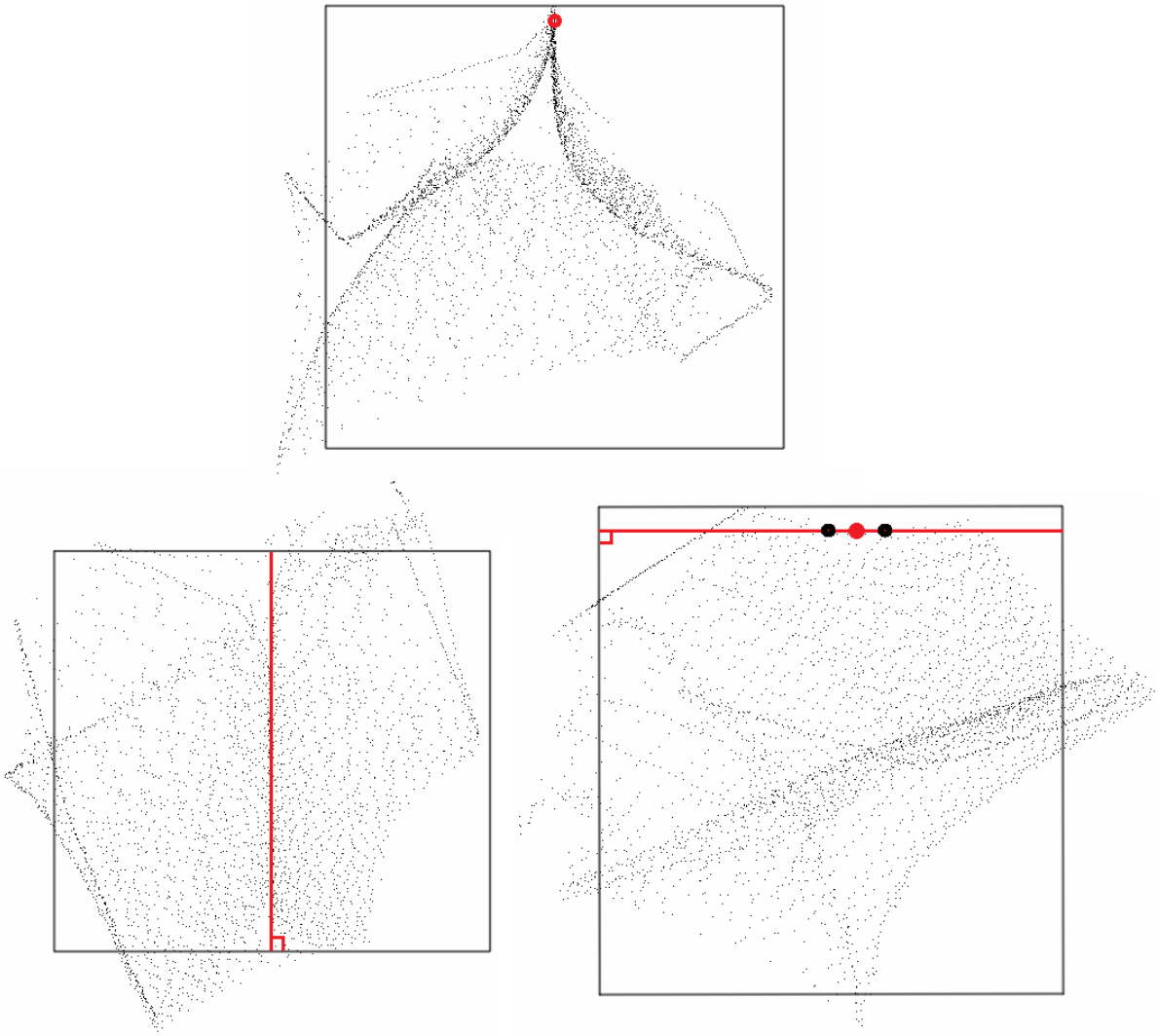

Figure 14. The microstructure is represented in 3D by a set of data points selected on 2D slices of the microstructure that were used to construct the 3D model. The three images show the desired orientation of the model after rotations have been performed. The top image shows a representation of the complete data set seen in the plane of interest for true dihedral angle analysis. The bottom left image shows that the line of sight is aligned with the direction of the tubule edge in which the dihedral angle will be measured. The bottom right image shows that two points on the edge on either side of the point in which the true dihedral angle will be measured (the red dot) are aligned with line of sight.

The first step in obtaining the correct plane for the creation of the 2D image is the rotation of the model such that the front view of the model in Imod is aligned with the normal of the plane of interest (Figure 15). In order to require the rotation, the model was rotated manually towards the desired orientation. The rotation needed for the alignment was then read from the controls menu in Imod. To finalize this step, the original model with all data points should be rotated to match the obtained rotations. This was done by modifying the text file for the original model with the cygwin command "Imodtrans -rz –ry –rx ". The rotations should be performed in this order to avoid errors.

The second step reduces the model to the relevant part only. The reduction step is important, as without such step a number of adjacent planes are projected onto the plane of interest, confusing the image. To do so, the model was extracted into a text file (model2point –scale [input.mod] [output.txt]) containing the coordinates of each of the points used to trace the contours of the microstructure in each of the slices of the slice & view series. The text file is used to select a model consisting of relevant points only. A the correction for slice thickness was performed by multiplying each of the z coordinates in the text file by the amount of pixels fitting within the thickness of a slice. The points of interest are those points with z-coordinate values within the range of the z-coordinates of the points used in the alignment. The text file was then converted to a 3D model with the "point2model –planar –scat" command in cygwin.

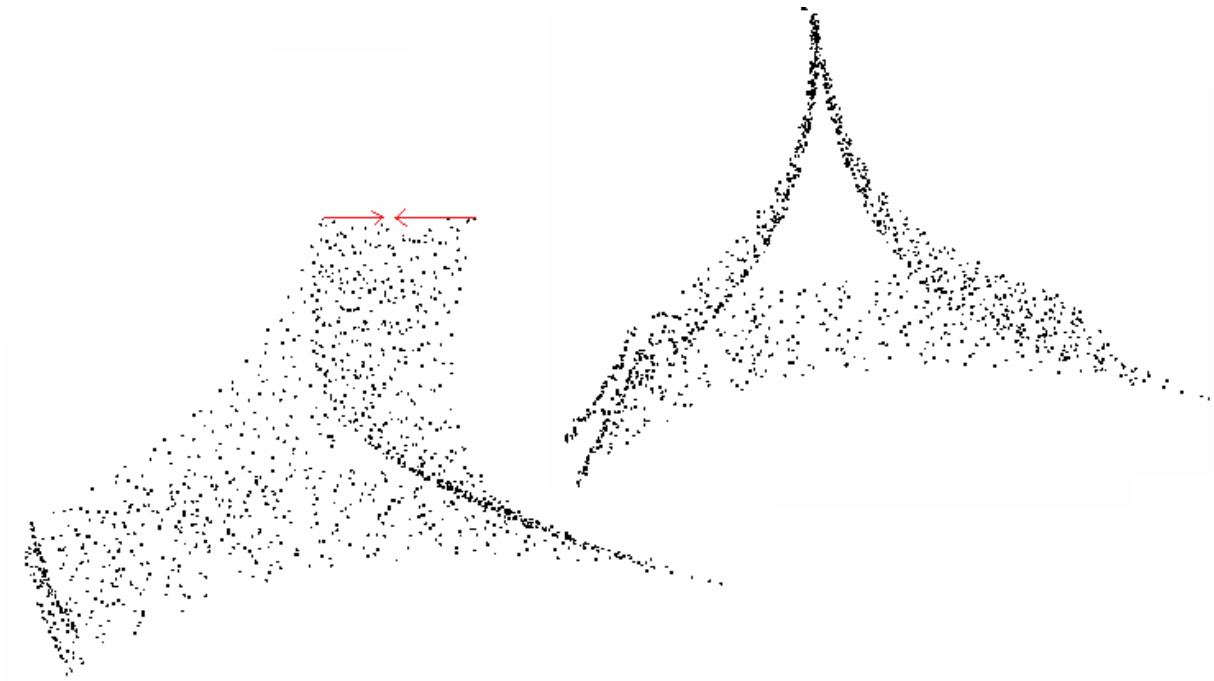

Figure 15. A reduction of the model is used for more accurate determination of the desired rotation of the model. The two points on equal distances of the point, in which the dihedral angle will be measured, in both directions, are aligned to obtain the rotation.

The next step is to isolate the geometry of the microstructure for analysis of the dihedral angle. After the rotation is performed, the point model is suitable for the modifications needed to determine the geometry of the microstructure in the plane of interest. To improve the quality of representation of the geometry by points, a selection was made of 100 data points with z-coordinate values as close to that of the plane of interest. This selection of points was then converted into a 3D model, after which it is compressed to a single plane. As a result of the earlier performed rotation, points that do not have the exact same z-coordinate value, are automatically projected along the normal onto the plane of interest during the compression. The resulting product is a 2D image of a set of points, together describing the geometry of the microstructure in the plane of interest. The produced 2D images were then analyzed with the dihedral angle program.

3.6.2. True dihedral angle (3D)

3D measurements of the true dihedral angle were performed at several points along one junction line or tubular edge (Figure 16). The variation of the dihedral angle is shown in table 7. This table shows average dihedral angle measurements in seven points lying next to one another. There is no clear trend in the evolution of the dihedral angle along the junction line. There is also no clear trend in the deviation from the average of the dihedral angle.

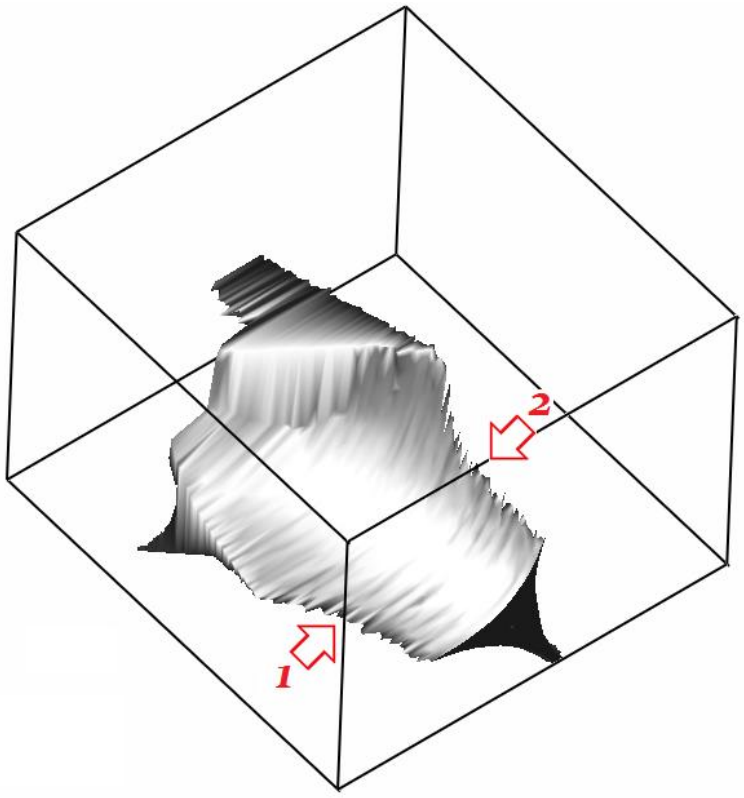

Figure 16. Measurements of the true dihedral angle were performed along the tubule edges pointed out by the arrows.

Edge 1	**1**	**2**	**3**	**4**	**5**	**6**	**7**
True dihedral angle	6,418	12,985	8,7	11,074	7,904	6,277	5,302
std. Deviation	3,1004	1,483	3,406	2,0576	3,5592	4,4824	2,1832

Edge 2	**1**	**2**	**3**
True dihedral angle	4,957	6,569	8,616
std. Deviation	2,1716	2,1348	2,3608

Table 7. Dihedral angles measured in several points along the tubule edges. Variations of the true dihedral angle can be observed along both tubule edges. The variation along edge 1 shows no continuous trend while variation along edge 2 does.

3.6.3. Validation of statistics

A set of cross-sections through a point with a known dihedral angle was generated. These random cross sections each represent the geometry of the microstructure, in a plane that is rotated from the plane in which the true angles lies, by an arbitrary rotation (Table 8). Rotations were first performed around the y-axis, followed by rotation around the x-axis. The original true dihedral angle was 11,07°. The last row of table 4 shows the difference of the measured apparent angle with the original true dihedral angle. The overall magnitude of the apparent angles is smaller than the true dihedral angle in most cases. However, some apparent angles show significantly larger values. A cumulative frequency plot of all apparent angle measurements can be seen in figure 17. The true dihedral angle was approached to within one degree by the mean of all apparent angles. The method of Gokhale & Zhang (2013) produced the same result. The median shows a larger deviation from the true dihedral angle.

rotations											
y-axis	5	5	5	15	15	15	25	25	25	45	65
x-axis	5	15	25	5	15	25	5	15	25	0	0
Dihedral angle											
	7,91	10,71	12,78	6,98	7,26	3,79	19,34	7,11	3,83	15,46	35,53
	12,88	13,27	13,7	10,52	12,25	9,9	12,68	13,85	2,84	9,09	36,01
	8,07	14,62	16,14	12,93	0	7,26	7,18	13,67	9,88	7,82	35,3
	5,93	7,07	8,58	9,75	0	8,95	8,53	14,06	8,21	14	43,65
	0	12,88	11,09	11,97	7,53	6,49	9,15	12,58	4,71	14,51	41,52
	6,83	5,66	5,73	3,83	12,42	7,1	2,26	15,96	5,18	11,39	36,07
	9,89	0	12,27	8,92	11,67	4,02	5,4	13,52	9,86	18,58	31,58
	12,24	2,89	4,73	9,24	4,12	10,35	11,24	6,16	5,74	19,53	16,73
	12,73	0	5,63	5,09	9,15	7,84	2,83	11,3	15,12	22,67	19,67
	13,48	5,01	4,43	14,7	5,9	0	11,55	14,75	11,03	17,85	35,92
mean	**8,996**	**7,211**	**9,508**	**9,393**	**7,03**	**6,57**	**9,016**	**12,296**	**7,64**	**15,09**	**33,198**
std. dev.	3,248	4,5272	3,688	2,581	3,62	2,396	3,776	2,4636	3,18	3,728	6,3228
difference	-2,078	-3,863	-1,566	-1,681	-4,044	-4,504	-2,058	1,222	-3,434	4,016	22,124

Table 8. All measurements of apparent angles performed on cross sections with varying orientation. The point in which the true dihedral angle is measured is the exact same point in which the apparent dihedral angles are measured. Apparent dihedral angles can be both larger and smaller than the true dihedral angle, which is ~11,1° in this case. [a] The difference between the mean dihedral angle and the true dihedral angle.

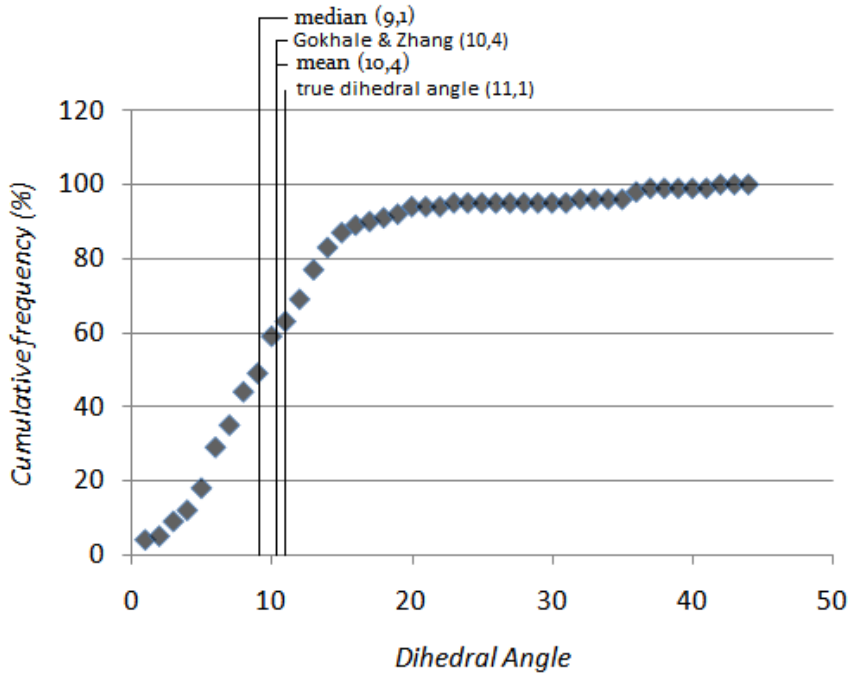

Figure 17. A cumulative frequency plot of all measurements performed for the extraction of 14 apparent angles shows a normal distribution around the obtained median.

4. Discussion

4.1. Magnification

The accuracy in measuring the dihedral angle is directly proportional to the quality of the images. The first measure for the quality of the images is the resolving power of the electron microscope. A higher resolving power means that more detail is recorded in the images. Another important factor determining the image quality is the signal-to-noise ratio, which is the ratio between the actual information from a sample and the noise level due to various sources. The ratio can be influenced by changing the beam current and scan rate. In addition, improvements of, mainly the detector technology has contributed to higher signal to noise ratios as well. A clear trend can be observed in older studies versus more recent work, being that more recent SEM studies usually result in lower dihedral angle values than older studies (Yoshino *et al.*, 2009). Such trend suggests that, considering improved technology and the corresponding image quality improvements results in higher measurement accuracy, dihedral angle values are smaller than originally assumed and that more recent studies give more viable results. TEM studies performed by Cmíral et al. (1998) at the highest possible resolution (0,5 nm) have resulted in dihedral angle values of 5-10°, which is in agreement with our results. Magnification, being independent of the previous factors, seems to have a direct relation with the image quality as well. The relationship is inverse and is related to limitations in distinction of detail at high magnifications.

The distinction of the grain boundary geometry is an important step in accurate determinations of the dihedral angle. The character of solid-liquid interfaces at the junction point attributes to some problems during dihedral angle determinations. However, this is inextricably connected with the magnification of the microstructure. An insufficient magnification potentially leads to the loss of essential detail concerning the geometry of the pore at the junction point in which the dihedral angle is determined. Such loss of detail can be attributed to two very different characteristics of the solid-liquid interface. The first being the occurrence of facets, where a single facet might have developed in such a close proximity to the junction point that it can only be seen at relatively high magnifications. The angle of the faceted interface with respect to the other interface will in this case be very different from an interface that is not faceted. When the crystal is isotropic, the grain boundary, and thus the solid-liquid interface will have developed a round shape. In this case the curvature of the grain boundary determines the dihedral angle in the junction at which both grain boundaries meet. The magnification can be of great influence in this case as well. Such issues pose limitations to the analyses performed with a universal stage (Holness; 2006). Studies on the true dihedral angle using this technique will only produce results at limited magnifications due to the use of optic microscopes, which have much lower resolutions than a conventional SEM and TEM. The

importance of higher magnifications or resolving powers can be linked to the fact that the curvature of grain boundaries causes them to curve away from each other in almost all cases. The accuracy of visual approximations of the tangents to the solid-liquid interfaces will increase with increasing magnitude. The effect of the magnification was demonstrated in figure 5a. The use of a simplified model in this case decreases the effects of observational errors linked to resolution or signal to noise ratio, as grain boundaries can be distinguished very clearly. Emplacement of the tangents closer to the junction point has a direct effect on the angle between the tangents, which will become smaller as the tangents are touching the grain boundary closer to the junction point. The same effect can be observed in measurements performed on real samples figure 5b. The increasing magnification of the images results in an apparent increase in the radius of curvature of the solid-liquid interface. Although changes in the radius of curvature along the solid-liquid interface do exist, apparent changes in radius of curvature still occur when the magnification is changed (Figure 5a). Real radii of curvature are obviously not influenced by changes in magnification.

4.2. 2D analysis tool

The importance of exact junction emplacement calls for a method that enables the determination of junction point with minimum interference from factors that are arbitrary. The method that was developed for analysis of dihedral angles in this study aims to avoid these factors by means of constructed junction points obtained by approaching the grain boundaries' shapes. Approaching the grain boundaries' shapes is straightforward in essence, but data points should be carefully selected. In general, the approach of the grain boundary by a mathematical shape could lead to errors if the shape of the grain boundary is not representable by a continuous mathematical function. The occurrence of anisotropy in the crystal grains is therefore of substantial importance and should be considered during analysis. Discontinuities in the shape of the crystal should be distinguished as these discontinuities act as boundaries for data point selection. Data points used to approach the grain boundary shape should be selected in only a single continuous 'segment' of the grain boundary. To obtain an accurate measurement of the dihedral angle, only the geometry of the grain boundary directly adjacent to the junction point should be taken into account (Figure 18). Properly selecting data points in this method requires distinction of the grain boundaries in the image, which is less susceptible to errors due to magnification. The constructed line, fitting the data points selected along the grain boundary, can be used to check the accuracy of the selected data set. Overall, a selection following the earlier described requirements, will result in a good fitting approach. The straightforward nature of both the selection and the assessment of the accuracy make the method very reproducible and unbiased, which contributes to a more reliable and continuous data set.

Another element of this method that contributes to a decrease in error due to arbitrary factors, is the construction of the circle describing the grain boundary. The center of the circle is determined for every three consecutive points. The average of the constructed centers is used as the center of circle used to approach the grain boundary. The radius is determined by taking the average of the distances between each of the centers and the coordinates used to construct them.

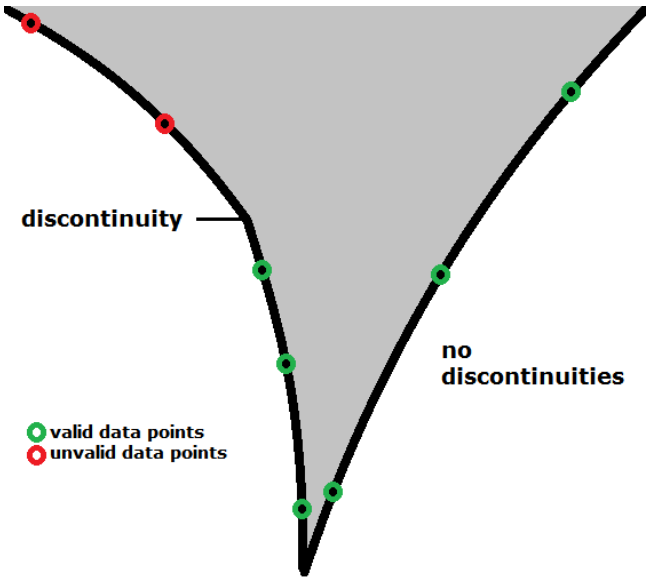

Figure 18. A representation of a junction point and two solid-liquid interfaces. Data points should be selected along a continuous part of the grain boundary that is directly adjacent to the junction point.

In case of a faceted grain boundary the grain boundary is straight. In this case the coordinates that make up the input of the program describe a straight line. The model, which is based on the attribution of circles to the different sets of coordinates, will construct a circle with an infinitely large radius. The curve of the circle will approach a straight line in this case, so the model will be valid for lines intersecting circles. The Young-Laplace equation (equation 1.4) justifies the attribution of an infinitesimally large circle to describe a flat (faceted) surface. A state of zero pressure difference is present at flat surfaces or interfaces. As the radii of curvature increase, the factor containing the radii of curvature will approach zero, eliminating the influence of the surface free energy and thereby equaling to zero pressure difference. In the case of two faceted grain boundaries, the model will not be able to calculate two intersection points. In this case, the coordinates should be entered in the section for faceted grains. This part of the model calculates the slopes of the lines that can be attributed to the coordinates and calculates the angle between the two lines in the same way as in equation (7.1).

The application of the 2D analysis tool on the images obtained from the 3D analysis, is in essence, the same process of data selection as with the original 2D images. However, careful data selection could require more time. The limited number of available data points for the selection reduces the clarity of the grain boundary geometry and makes discontinuities in them less distinguishable. Each point present in the 2D image however, is valid for selection as they are points that were initially chosen to describe the grain boundaries during construction of the 3D model. In both cases, the constructed circles and lines can be used to check the accuracy of the measurement by qualifying the synchrony of the circles and lines to the grain boundary.

4.3. Measurement accuracy

The accuracy of the measurements can be influenced by varying factors e.g. resolution of images and decrease in precision of coordinate selection associated with this. Because of the general issues associated with dihedral angle measurements, an apparent dihedral angle in a 2D section of a (natural) sample cannot be determined with any degree of certainty. The lack of an exact measure for comparison of results could cause implications when the method used is not properly tested. The actual data involves images with limited spatial resolution and noise, which potentially influences the accuracy as well. In order to make an assessment of the accuracy of the software tool, a series of analyses were performed on a object of which the influence of previously described factors is minimized. The accuracy of the software tool is established based on the measurement of a known artificial dihedral angle, effectively providing a value for comparison of results. The perfect shape of the grain boundaries eliminates influences caused by minor discontinuities in the grain boundaries that might be overlooked by the operator. Furthermore, the representation of the grain boundary by a solid line provides a well-defined target for coordinate selection, thereby minimizing possible deviations from the grain boundary caused by insufficient resolution in the images. However, minor errors caused by inconsistency and lack of precision in the selection process of the operator cannot be eliminated. The standard deviation of the results from measuring the same dihedral angle gives insight in the reproducibility and accuracy of the tool. The difference between the actual dihedral angle and the average measured angle based on a data set of 20 measurements was only 0,73°. The average standard deviation of the measured dihedral angles is 1,2°. Accuracy of the tool under optimal conditions can therefore be set at approximately 1-2°, which is significantly less than the 5° inaccuracy presented by Cmíral *et al.* (1998) using TEM.

4.4. 3D dataset

4.4.1. Data modification - rotation

Rotations of the model were performed to allow for further analyses. Results were visually compared to the manually rotated model. The spread of data points in the new model, with zero rotation, should be equal to that of the old. Rotation of the stretched model about the different axes in order of x,y,z, did not gave a good result. Rotations performed in the order of z,y,x, did result in the desired rotations as the spread of data points was exactly the same as in the old model (figure 19), now with the z axis aligned with the line of sight.

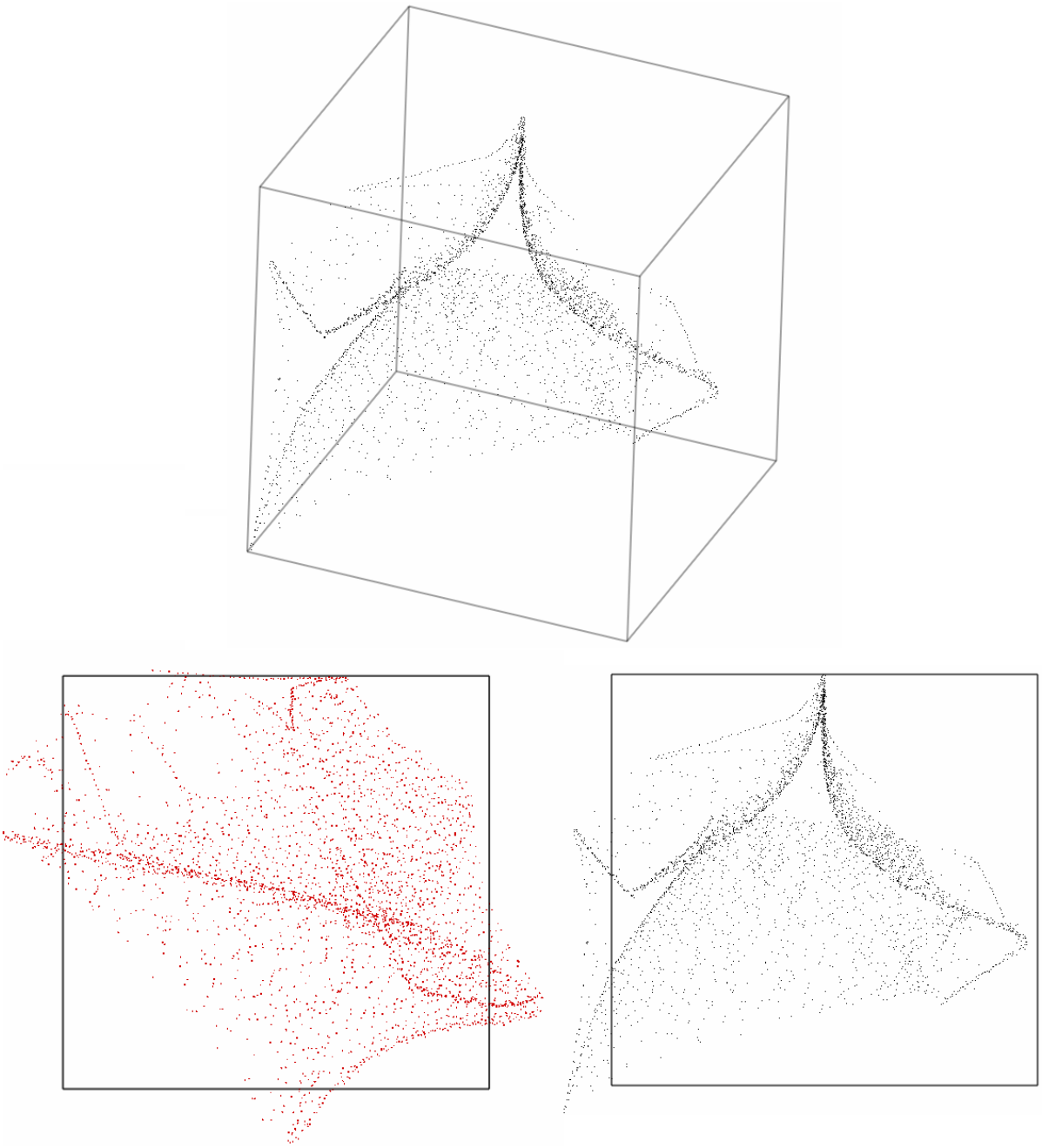

Figure 19. The order of rotations around different axes is important for the final result. The top image shows the original model with a manually selected rotation. The bottom left image is the result of a rotation of the model in order x,y,z, which does not compare to the distribution of data points in the original model. The bottom right image is the result of rotation of the model in order z,y,x, which results in an identical data point distribution.

4.4.2. 2D representation

For the production of a 2D representation of the microstructure in the plane of interest, a selection of data points was made. In order to get a good 2D representation (Figure 20a), this selection should contain a sufficient number of data points with z-coordinate values close to that of the plane of interest. Since, the data points that do not lie in the, plane were automatically projected onto the

plane when looking along the z-axis. The amount of data points used to construct the 2D image should be sufficient enough to provide a good representation of grain boundary. Discontinuities in the grain boundary should be distinguishable as well. Overall, a selection of 100 data points resulted in images that gave a sufficient description of the grain boundary geometry in the plane of interest (figure 20b).

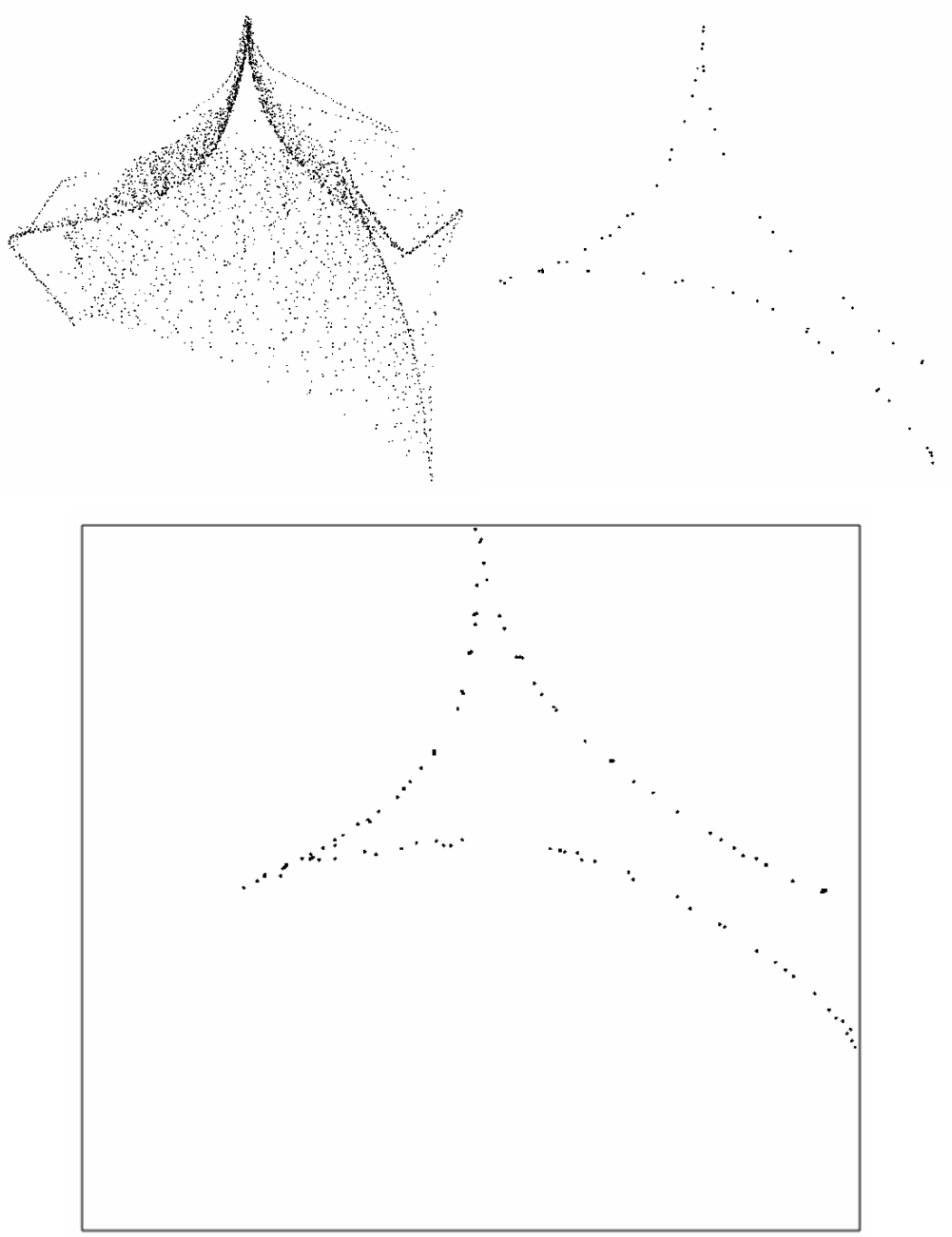

Figure 20.a. The top two images show the original model after rotation and a 2D representation of the model. The model was filtered for points with z-coordinate value within a range surrounding that of the plane of interest resulting in a representation of the geometry in this plane. **b.** Selecting 100 data-points results in a 2D representation with sufficient data resolution.

4.4.3. Measurement quality

The measure of reproducibility of the measurements performed on the 2D representations of the microstructure is not as good as it is for that of the 2D analyses of the original 2D SEM images. However, the number of measurements this was based on is far less compared to that of the original 2D SEM images. Only 16 angles were taken into account here, these include the ones used in the variations and rotation sections. Ten measurements that were performed on each of these dihedral angles resulted in an average standard deviation of 3,1° for separate dihedral angles. The description of the grain boundaries in the analyses did in most cases run through the data points present in the 2D image (Figure 21). The number of points lying along the line or circle is an important measure of the quality of the measurement. It can also be used to distinguish discontinuities in the curvature of the grain boundary. The image obtained in each analysis should therefore be inspected carefully. The presence of discontinuities and irregularities can then be taken into account during following analyses, honoring the basic guidelines for data point selection described earlier. An example of a measurement performed on a constructed 2D cross section of the 3D model can be seen in figure 6. The yellow circle approaches the grain boundary in the top image very well as all the data points in close to the junction point lie either on the circle or close to it. A well distinguishable deviation of the data points from the circle can be observed in the lower part of the grain boundary. The onset of the deviation from the circle can be interpreted as a discontinuity in the curvature of the grain boundary, which might be associated with evolution of a facet.

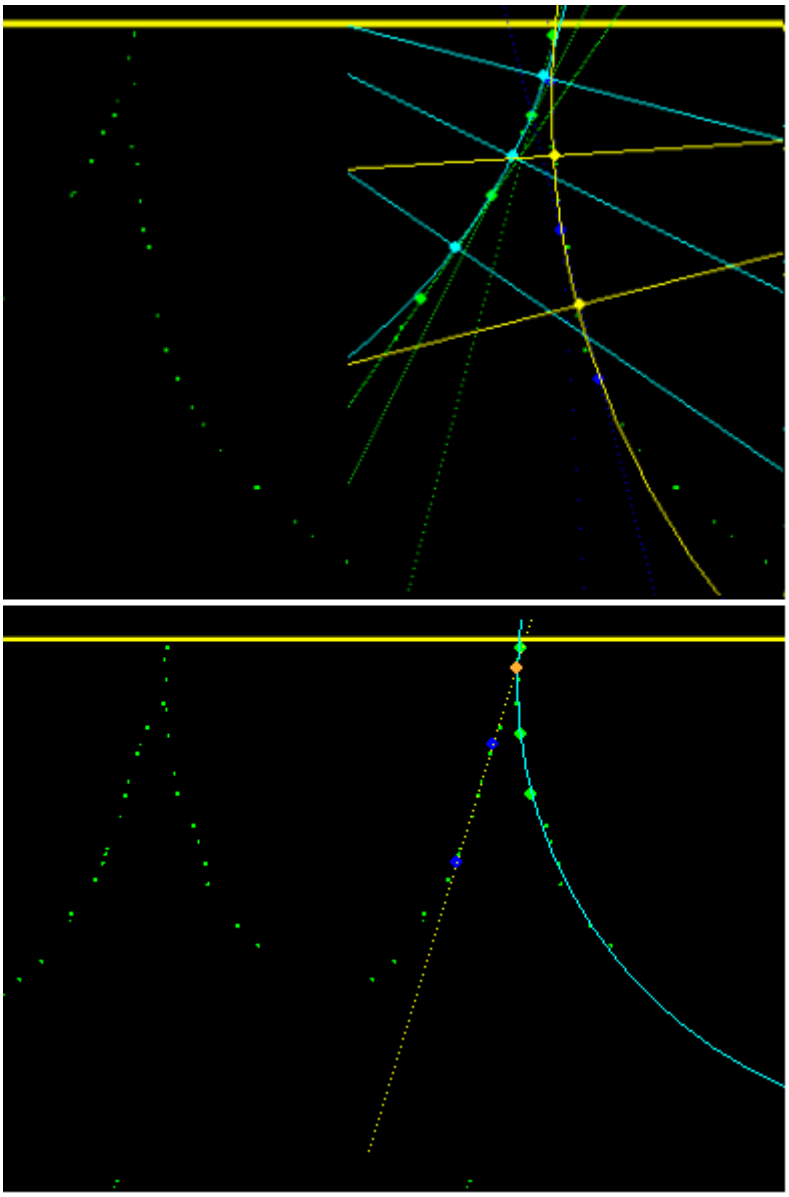

Figure 21. The top image shows an example analysis of a dihedral angle between two curved solid-liquid interfaces. The bottom image shows an example analysis of a dihedral angle between a curved interface and a faceted interface.

4.4.4. 2D vs 3D statistics

Another problem associated with dihedral angle measurements is the extraction of the true dihedral angle. The nature of most datasets used dihedral angle analyses is that they consist of a series of 2D images. These images represent random cross sections through a sample and through the microstructures present in that sample. Since the true dihedral angle is a unique angle for any part of a microstructure, it can only be measured when it lies in a particular plane. Random cross sections through a microstructure will therefore not hold direct information about the true dihedral angle in most cases. Measurements performed on random cross sections will yield what are called apparent

angles. Several statistical methods have been suggested by multiple authors, which can be used to approach the true dihedral angle based on a set of apparent angles. The majority of suggest the use of the median in olivine melt studies (e.g. Holness, 2006; Yoshino *et al.*, 2010). A normal distribution of true angles around the median value of apparent angles was suggested to be most likely as solid-liquid interfaces are influenced by anisotropy in the crystal leading to a variety of true angles *(Jurewicz & Jurewicz; 1986)*. However, the authors also stated that these distributions could also be the result of measuring errors, which could be significant (5-10°) when manually selecting tangents to the solid-liquid interfaces. Possible distributions of true angles would be either relatively continuous or the values of true angles should be closely clustered as no bimodal distributions were observed in the studies of Jurewicz & Jurewicz *(1986).* Gokhale & Zhang(*2013)* suggested that even when a such a distribution of true angles exists, the mean value of the population of apparent angles observed in IUR 2D planes would be equal to the mean value of the distribution of true angles in the microstructure. Then if the true dihedral angle distribution could be represented by a 2D distribution function , the mean and the variance of the distribution can be calculated by equations (1.5) and (1.6) The importance of the mean value of the apparent angle distribution is emphasized by the fact that the median and the mode of the apparent angle distribution are often biased due to skewed distributions, causing inequalities between the mean, median and mode (*Goodwin et al.; 2009*). In this study a set of apparent dihedral angles of one true dihedral angle was produced. The data shows that the apparent angle can be larger as well as smaller than the true dihedral angle, depending on the orientation of the cross section. The cumulative frequency curve of the apparent angles shows a normal distribution of apparent angles around a median of approximately 9° with some skewing at larger dihedral angle values. Both the mean (10,44°) and the method presented by Gokhale & Zhang (2013) (10,42°) taken over the complete 3D dataset gave a better representation of the true dihedral angle (11,1°). The skewing represents a lower number of high value dihedral angles. The selection of rotations used for the production of cross sections was random and heterogeneous. This has resulted in larger apparent angles in only a small portion of the cross sections. A more homogenous selection of rotations for cross sections will probably result in a normal distribution of apparent angles.

4.4.5. Variation

The continuity of the dihedral angle along a tubular edge of a melt pocket was studied. A continuous dihedral angle value could be expected based on equation 1.2 (Smith, 1964) and the Young-Laplace equation (1.3), provided that there are no variations within the individual crystals, that could influence the surface free energy, and no pressure variations within the melt. The attribution of true dihedral angle values based to several points along a tubular edge should provide diagnostic results

about any variations present. No high data resolution is required to detect variations. The results showed no well distinguishable trend in variation at a resolution of seven data points in edge 1 (Table 7a). This was supported by the lack in a variation trend in the standard deviations of each of the dihedral angles. The three dihedral angles measured along edge 2 do show a trend (Table 7b). However, variations in the dihedral angle are within the margin of error. These small variations, in combination with the small number of measurements performed along edge 2 , leaves room for coincidence. The absence of continuity in any form, either in variation or in the absolute form, could be the consequence of several factors. Although there is no continuity along the tubular edge, a significant amount of variation can be observed. Variations in the dihedral angle values occur at a small scale and are chaotic. Although most of the variations could be attributed to measurement errors, some variations are too significant and might be the influenced by other factors. The abrupt changes in the dihedral angle on small scales could be the result of small scale processes affecting local free energy configurations. Isotropic systems are relatively simple systems that can easily be described by equations 1.2 and 1.3, due to the lack of variations in the crystal that are of influence on the energy configurations e.g. variations in crystal lattice orientation. The system can therefore be treated as a unified whole on a larger scale. The presence of anisotropy has obvious consequences for the energy distribution and can be treated as a viable cause for the variations in dihedral angle observed along the tubular edge. The process of surface diffusion applied to the evolution of facets could explain variations in influential parameters on a very small scale (Carter *et al.*, 1995). Surface diffusion can result in merging and stepping of facets. Stepping is the replacement of one facet by two collinear facets with a combined length equal to that of the original facet. These facets are connected by a zero-length facet of zero weighted mean curvature (Carter *et al.*, 1995). These processes, which involve the elimination and production of facets, are gradual, as well as their effects. The shrinking of facets to atomic proportions that is linked to their elimination, and the production and growth of new facets can result in anisotropy at all scales. The question arises if the method that is presented provides the resolution required to identify such elements. The current accuracy and quality of the 2D representations combined results in error margin that covers a significant portion of the range of variations observed. Further development of the technique should therefore focus on increasing the resolution of the data in the acquired 2D representations of the 3D model.

4.5. Mean vs median

The median and the mean of the measured dihedral angles for each sample were compared. For places in which melt is separating two grains and thereby connecting to melt pockets, a 0° dihedral angle was recorded. Separate values were determined for a selection of angles including and excluding 0° dihedral angles. The results are shown in table 9.

melt content	mean	mean no 0°[a]	median	Median no 0°[a]
10%	6,61	7,97	6,39	7,47
5%	12,47	25,80	0,00	18,34
3,5%	6,43	11,20	4,01	9,46
2,5%	44,68	46,56	38,28	41,47

Table 9. [a] No 0° dihedral angles were taken into account here.

Comparison between the median and the mean of each samples shows that the overall value of the median is lower than the mean value. This corresponds to earlier results that were compiled by Holness (2006). The difference between the median and mean values of the samples does not seem to be affected by the presence of 0° dihedral angles. The zero value median of the E1 sample can be attributed to the small number of measurements performed in this sample in combination with a relatively large number of 0° dihedral angles. The number of 0° angles present in the sample could affect the median of a sample severely. The E1 sample shows a wide range of dihedral angles that contribute to a relatively high mean dihedral angle. However, the median of the sample is zero, which can be attributed to the large number of 0° dihedral angles observed in the sample, which is related to the large amount of connected melt pockets present in the sample. The inclusion of 0° dihedral angles could therefore cause a significant error in the results. Such errors should be considered when using the median as a measure for the true dihedral angle. The distribution of the apparent angles as plotted in the cumulative frequency plots in figure 10a and 10b has a normal shape for both the F1 and the A3 sample. The normal distribution patterns of these samples support the validity of the datasets. The data suggests that the true dihedral angle in the case of these samples is best approached by the mean value of dihedral angle measurements rather than the median. Representation of the true dihedral angle by the median is especially poor in samples with a high zero degree dihedral angle versus non-zero degree dihedral angle ratio as the non-zero degree dihedral angles could become irrelevant. The mean should therefore be considered to be a viable statistical approach of the true dihedral angle in materials that have a significant amount of connected melt pockets or melt layers.

4.6. Melt pocket size

The size of the melt pockets in the different samples was not measured quantitatively. However a qualitative estimation of their sizes can be made. The general relationship between the size of the microstructures and the magnifications necessary for optimum image quality is considered here. There seems to be no direct linear relationship between the magnification and size of the microstructures and the melt content of the samples. At low melt content, the size of the melt pockets is very small. When the melt content increases, the size of the melt pockets initially shows a drastic increase after which a slow decrease in melt pocket size sets in. A possible explanation for this relationship between microstructure size and melt content could be that the microstructures in the G1 sample are very small because there is little melt available in the system. The grain size in the in the G1 sample is smaller as well, which results in a larger number of smaller melt pockets. As the number of melt in the system increases towards 3,5% in the A3 sample, more melt has accumulated in the melt pockets and their size has rapidly increased. Due to the production of more melt in the system, more wetting will occur and the connectivity between melt pockets will increase. The increase in connectivity, effectively causes a spread of the available melt over more melt pockets causing the existing melt pockets to decrease in size. Melt pockets will decrease in size as this process continues towards the point at which the system has a 10% melt content in sample F1. Insufficient data was available to determine a possible relationship between the final grain size and the melt pocket size or dihedral angle.

4.7. Dihedral angles and melt content

No clear relationship between the melt content and the average dihedral angle can be seen in the data. Average dihedral angles corresponding to a melt content of 10% are relatively low. The average dihedral angle for the 5% melt is approximately 6° higher. However, the dihedral angle associated with a 3,5% melt content is approximately the same as that of the sample with 10% melt content. The number of measurements performed, as well as the number of different angles taken into account for both the F1 and the A3 samples, are considerably larger than those for the E1 sample. The average dihedral angle obtained for the G1 sample (2,5% melt content) really stands out at approximately 45°. Such a high average dihedral angle is can be linked to textural equilibration of the sample. The process of textural equilibration of a rock results in a configuration of the melt-filled pore structure between two end members at any given time (Holness *et al.,* 2005). The initial state in which the grain shape is dominated by growth processes, solid-solid-melt dihedral angles have a median lying at approximately 60° and a relatively high standard deviation. Equilibration of the rock towards melt-present equilibrium then results in an evolution towards a lower median and a lower

standard deviation (Figure 22, Holness *et al.,* 2005). The results also show the same relation between the average dihedral angle and the standard deviation. High dihedral angle values in the G1 sample could therefore be explained by a small degree of textural equilibration with respect to a higher degree of textural equilibration in the other samples. Considering the amount of melt in each of the samples, there could be a relationship between the amount of melt added to the system and the degree of textural equilibration as well.

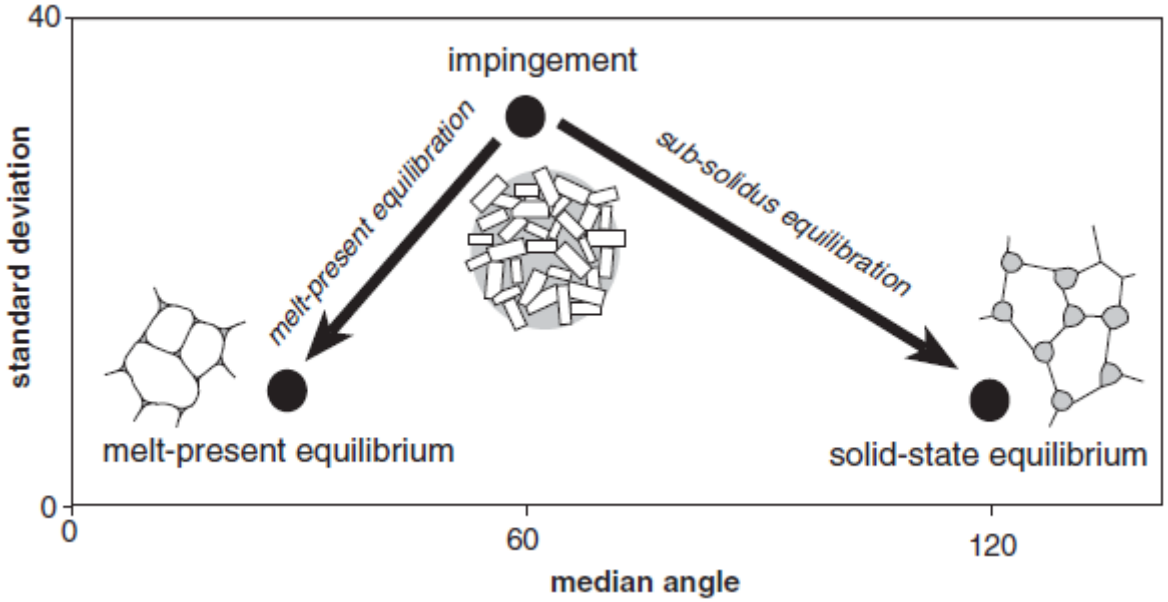

Figure 22. The solid-solid-melt dihedral angle population evolves from one with a median of approximately 60° and a high standard deviation towards one with a lower median and standard deviation when melt-present equilibrium is achieved. (Holness *et al.,* 2005)

All samples show dihedral angle values of <60° and are therefore typical for silicate mineral melt pairs (Holness *et al.*, 2011). The variation in dihedral angle with varying melt content is irregular. Another factor that could be of influence on this is faceting of the grain boundaries. The wetting of grains in systems that have experienced faceting is systematically lower than no faceting systems (Yoshino *et al.*, 2005; Yoshino *et al.*, 2006). Since wetting is directly related to the dihedral angle, faceting could be a cause of irregularities in the trend of dihedral angle values. The results indicate that faceting could play a role in the E1 sample in particular. The proportion of dihedral angles between significantly faceted grain boundaries versus dihedral angles between more isotropic grains is significantly larger than in the F1 and A3 samples, with 67% for E1 and 45% and 53% for F1 and A3 respectively. The faceted angles in the E1 sample also contribute more to a larger average dihedral angle for the entire sample than those in the other samples (Figure 9). The large factor 2,07 describing the proportions between the magnitudes of the average faceted angles versus the average no faceting angle supports this statement. However, when only no faceting dihedral angles were taken into account, a similar variation in each of the earlier described sample characteristics

can be observed as well. The trend in dihedral angle data in the case of the no faceting angles has less extreme fluctuations. The observed variation in the radius of curvature of the grains with varying melt content could have caused such a similar trend (Figure 11). The data shows a slow increase in the mean radius of curvature of non-faceted grains between which dihedral angle measurements were performed. An increase in the range of radii of curvature can be observed as well, with a very large range of radii of curvature being observed in the 10% melt sample. The large values represent grain boundaries that belong either to very large grains or to grain boundaries that have developed discontinuities, marking the boundaries between areas with different radii of curvature. These areas appear to be underdeveloped facets. Variations in grain size cannot explain the observed range in radii of curvature. Although, the discontinuities could act as boundaries between individual facets, these were not treated as such due to the presence of curvature. However, a part of a grain boundary with an extremely large radius of curvature approaches the geometry of a facet and could therefore have a similar effect on dihedral angle data. Measurement errors could also explain the fluctuations in the average no faceting dihedral angle values as the fluctuations are no more than twice the error margin set for the measurement method. Also, some faceting could have been misinterpreted or not taken into account entirely due to limitations in the resolution of the imaging. The number of dihedral angles contributing to the average no faceting dihedral angle in E1 is very low as well. An unfeasible average no faceting dihedral angle value could be the result of either one or a combination of such factors. The fluctuations in the average faceting dihedral angles cannot be explained by measuring errors. Possible changes in the amount of faceting might cause the irregular variation of dihedral angle with melt content. However, more research is needed in order to be conclusive about this subject.

The range of dihedral angle values per sample varies sufficiently as well. These variations seem to be proportionate to the variations found for the average dihedral angle. Samples F1 and A3 show a relatively small standard deviation of dihedral angle values from the mean value with respective standard deviations of 3,8° and 6,27°. The range of obtained dihedral angle values is larger for the E1 sample, which shows a standard deviation of 15,45°. The G1 sample tops the list with a standard deviation of 25,05°, which translates to a large range of angles found in that particular sample. However, the G1 sample statistics were based on the large number of measurements. The variations of the observed range of angles and of the average dihedral angle with varying melt content are very similar. Systems with faceting commonly experience heterogeneous liquid distribution. Heterogeneity is expressed in a decrease of liquid-phase fraction in melt tubes and the development of large pores and clusters of pores (Yoshino *et al.*2005). Such clusters of pores were observed in the

E1 sample only. The presence of larger pores and the decrease in the fraction of the liquid phase, associated with heterogeneity, causes a decrease of migration of the melt in between pores, effectively increasing dihedral angles at those junction points. This is related to the extension of tubule edges of tubular melt pockets into grain boundaries with increasing melt fraction (Wark *et al., 2003).* If part of the melt pockets would be subject to such changes, it will result in an increase in the range of angles present in the sample. Heterogeneity in liquid phase distribution could therefore be a valid cause for an increase in the observed range of angles in the E1 sample.

Yoshino *et al.* (2007, 2009) studied variations in the dihedral angle with varying pressure and temperature and suggested that a decrease in the dihedral angle can be associated with increased temperatures. The pressure dependence of the dihedral angle can be attributed to an increased solidus temperature with increased pressure. Studied effects at near solidus temperature at different pressures, showed that the increase in temperature necessary to attain the solidus temperature at higher pressures causes further decrease of the dihedral angle to nearly 0°. Overall, an increase in temperature will lead to achievement of solidus-temperatures at an earlier stage, resulting in an increase in melt. This validates our results, which show a general trend of decreasing dihedral angle with increasing melt content. However, the samples from ten Grotenhuis (2004; 2005) used in our study were heated to 1450 - 1475°C and were not pressurized. These samples initially contained 5% enstatite, which were only preserved in the sample with low melt content (2,5%), while no enstatite grains were observed in sample with higher melt contents. At around 1475°C and under atmospheric pressure, the forsterite in the samples does not reach its solidus (Philpotts, 2009). The presence of enstatite grains in the low melt content samples and their disappearance with increasing melt content could be the product of incongruent-melting of the forsterite-enstatite system. High dihedral angle values in the low melt sample could thus be explained by the presence of enstatite grains. The removal or dissolution of the enstatite grains in the samples with higher melt content, results in a decrease in the dihedral angle values due to an increase in the melt content as well as the removal of the larger enstatite-enstatite-melt and enstatite-olivine-melt dihedral angles with respect to olivine-olivine-melt dihedral angles (Holness, 2006). Although the large dihedral angle in the G1 sample could be explained by the presence of pyroxene grains, the low dihedral angle values in the samples with higher melt content can not necessarily be explained by the absence of pyroxene grains. The samples have not been subjected to temperatures and pressures associated with such an extreme decrease in dihedral angle values (Yoshino *et al.* 2009). The very low dihedral angles recorded could be the result of a small amount of quench growth (Yoshino *et al.* 2005).

4.8. Cumulative frequency plots

Cumulative frequency plots show the distribution of apparent dihedral angle populations. The apparent dihedral angle distributions of all samples show curves, very close to normal distribution curves. Deviations from the normal distribution in all plots are due to positive skewing, resembling the results of many studies combined by Holness (2006). The amount of skewing varies per different cumulative frequency plot and is caused by a relatively high abundance of low value dihedral angles in the samples. Although the difference is small, the deviations from the normal distribution are less profound when no 0° dihedral angles were taken into account. Such deviations have manifested in all samples containing any number of 0° dihedral angles, but to a greater extend in the E1 sample in which a large number of 0° angles were observed. The cumulative frequency plots of the F1 and A3 samples show normal distribution patterns (Figure 10a and 10b). Very small changes in the distribution curves of these samples between the plot for faceted angles and the plot for non-faceted angles (Figure 10c and 10d) suggest that the effect of faceting on the distribution of apparent angles is minimal in these samples. The curves in the cumulative frequency plots evolve towards the new median value from the plot for faceted dihedral angles to the plot for non faceted dihedral angles. The distribution curves of the E1 and G1 sample show larger deviations from normal distribution curves in the plot for all angles. Both deviations can be characterized by positive skewing in the lower segment, and negative skewing in the upper segment of dihedral angle values. Although a certain degree of positive skewing is a common phenomenon in dihedral angle measurements (Holness, 2006), which justifies the deviations in the lower segment of the G1 sample, the positive skewing in the lower segment of E1 can also be explained by a large number of 0° angles. The negative skewing present in the upper segment of the dihedral angle values is a manifestation of a decrease in the amount of large dihedral angles as well as the presence of a very small amount of extremely large dihedral angles. Similar negative skewing of dihedral angle data has been reported by Yoshino *et al.* (2010). Their results showed clear deviations from theoretical curves when apparent angles were large. These types of deviations from normal distributions could be the result of the presence of a normal distribution of true dihedral angles (Jurewicz & Jurewicz, 1986). Deviations become more distinct with increasing standard deviation. The deviations observed in the E1 and G1 sample are more distinct in the plot for the faceted grains, while the plot for the non faceted grains clearly shows an evolution of the curves towards a normal distribution along curves matching the respective mean values for non faceted angles of ~10° and ~40° of each of the samples. The decrease in deviation from the normal distribution curve suggests faceting has a major influence on the distribution of apparent dihedral angles. The large proportions of angles measured between faceted grains in the E1 and G1 samples support this. Excluding faceting as well as 0° degree angles results in

a more normal distribution of the 2,5% melt sample (Figure 10e). The 5% melt sample also shows a more normal distribution compared to the other plots, which can be attributed to the large amount of faceting as well as 0° angles present in the sample that are excluded in figure 10e. The amount of data however, is insufficient to draw conclusions from.

4.9. CL imaging

Cathodeluminescence imaging of the samples revealed the presence of a significant amount (~10%) of pyroxene in the G1 sample (Figure 6a). Pyroxene is absent in the other samples, which could suggest that the pyroxene has dissolved in the melt in the samples with higher melt content. The A3 and E1 samples both show melt with high CL intensity relative to the grains in the samples, which could be caused by a pyroxene-enriched melt (Figure 6c and 6d). The grains in both samples show a rim with higher photon emission. The most important observation, the disappearance of pyroxene when melt content increases above 2,5%, could be associated with the large dihedral angle values in the G1 sample. The presence of pyroxene minerals could have affected a certain number of the dihedral angle measurements in this sample as the changes in minerals strongly affect the energy configuration at triple junctions by changes in the surface free energy. Increased dihedral angle values due to the presence of pyroxene were suggested by Toramaru and Fujii (1986). The enrichment of the melt in pyroxene could have similar effects in the other samples as well. Mineral chemical zoning is a possible cause for the evolution of such rims. Another possible cause for high CL intensity is the presence of Al due to addition of the melt to the samples. Aluminum is highly compatible in forsterite as well as enstatite, which are both rich in magnesium. The bright rims of the grains might be the result of increased Al-content in the rim. The original grains contained no Al. The incorporation of Al during crystal growth could cause mineral chemical zoning. Mineral growth might have occurred during quenching or during multiple heating experiments (ten Grotenhuis *et al.,* 2004; ten Grotenhuis *et al.,* 2005). The formation of Al-rich rims by mineral growth is supported by the fact that no rims are observed in the sample with the smallest grain size (G1). As increasingly more Al becomes incorporated in the crystal grains, the melt will slowly become Al-depleted. The Al-depletion of the melt causes increased contrast in CL intensity between the grains and the melt. The presence of wider rims as well as an increased CL intensity contrast in samples with higher melt content might suggest a higher degree of mineral chemical zoning and/or quench growth has occurred in these samples. The very low dihedral angles measured in these samples might be influenced by this phenomenon as suggested by Yoshino *et al.* (2005). However, measurements of the melt composition are needed to be conclusive about this.

5. Conclusions

In this study the relationship between the 3D true dihedral angle and the distribution of 2D apparent dihedral angles has been studied in a series of olivine samples with varying melt content. Visual approximations of tangents used to measure the dihedral angle between two grains are strongly influenced by magnification and resolution of images. A new method has been developed that provides mathematical handles for dihedral angle measurements by approaching grain boundaries based on the selection of data points along the grain boundary, thereby minimizing errors related to the highly arbitrary process of estimating tangents manually. Results can be tested quickly and easily, which adds to their validity. The method is compatible with constructed cross sections of 3D microstructures produced in this study, although precision of measurements decreased from ~1° to ~3° due to the limited amount of data points in the cross sections. True dihedral angle data suggests that a variety of true dihedral angles could exist within a single system. However, no diagnostic results for a continuous trend in variations of the true dihedral angle have been observed along a single tubular edge. The true dihedral angle was evenly well approached by the mean value and the method by Gokhale & Zhang (2013), which approached the true dihedral angle to within a single degree. The median showed a larger deviation from the true dihedral angle but not significantly. Analysis of the 2D data in cumulative frequency plots showed normal distributions of the apparent angles around values approaching the mean rather than the median which supports the 3D data. Deviations of the median are mainly caused by the presence of connected melt pockets and associated zero degree dihedral angles. Faceting is another major influence on the distribution of apparent angles as well as their individual magnitudes. The 2,5% melt and the 5% melt samples from ten Grotenhuis et al. (2004), both contain large ratios of faceted grains to non-faceted grains and both show deviating results from the 3,5% melt and the 10% melt samples. The 2,5% melt sample shows the largest difference in dihedral angle values. CL imaging suggests that the presence of enstatite grains could be of major influence on the dihedral angle values observed in the 2,5% melt sample. The presence of bright rims in CL imaging of the samples with high melt content, in combination with low dihedral angle values, could suggest that quench growth occurred in the samples. However, chemical analysis of the melt is necessary to be conclusive about this. In general, the data suggests that the olivine-melt dihedral angle is lower than 20-50°, as suggested in previous SEM studies. Based on the results of this study, true dihedral angles ranging between 0-15° are most viable in the olivine-basalt system.

Acknowledgements

I am grateful to Chris Schneijdenberg for introducing me to the Phenom tabletop SEM, thereby teaching me the basics of SEM use. Tilly Bouten is also acknowledged for sharing her knowledge in XL30 SEM use, allowing me to collect data independently. I would also like to thank dr. Saskia ten Grotenhuis for providing the forsterite samples. Professor dr. Martyn Drury is acknowledged for giving me the opportunity to do this research and for his guidance throughout the research. Finally, Matthijs de Winter, with his infectious passion for electron microscopy, is thanked for lively interdisciplinary discussions and intensive support and guidance. All have hereby contributed to the widening of my academical horizon, for which I am very grateful.

References

Cahn, J.W., and Handwerker, C.A., Equilibrium geometries of anisotropic surfaces and interfaces, *Materials Science and Engineering, A162, pp 83-95*, 1993.

Carter, W.C., Roosen, A.R., Cahn, J.W., and Taylor, J.E., Shape evolution by surface diffusion and surface attachment limited kinetics on completely faceted surfaces, *Acta metall. mater. Vol. 43, No. 12, pp 4309-4323,* 1995.

Cmíral, M., Fitz Gerald, J.D., Faul, U.H., Green, D.H., A close look at dihedral angles and melt geometry in olivine-bassalt aggregates: a TEM study, *Contrib Mineral Petrol 130: pp 336-345,* 1998

Felberbaum, L., Rossoll, A., Mortensen, A., *a* stereoscopic method for dihedral angle measurement, *Journal of Materials Science 40, pp 3121-3127*, 2004.

Gokhale, A.M., and Zhang, S., Stereology of microstructural dihedral angles in three-dimensions, *Microsc. Mircoanal. 19 (Suppl 2),* 2013.

Goodwin, W.B., Bharadwaj, M., Mao, Y., Gokhale, A.M., Gurumurthy, A., and German, R.M., Estimation of three-dimensional mean dihedral angle in W-Ni-Fe alloy liquid-phase sintered in microgravity, Scripta Materialia 61, pp 1101-1104, 2009.

ten Grotenhuis, S.M., Drury, M.R., Peach, C.J., and Spiers, C.J., Electrical properties of fine-grained olivine: Evidence for grain boundary transport, *Journal of Geophysical Research, Vol. 109, B06203,* 2004.

Harker, D., and Parker, E.R., Grain shape and grain growth*, Transactions of the American Society of Metals 34, pp 156-195,* 1945.

ten Grotenhuis, S.M., Drury, M.R., Spiers, C.J., and Peach, C.J., Melt distribution in olivine rocks based on electrical conductivity measurements, *Journal of Geophysical Research, Vol. 110, B12201,* 2005.

Herring, C., Some theorems on the free energies of crystal surfaces, *Physical Review, Vol. 82, No. 1, pp 87-93,* 1951.

Hier-Majumder, S., and Abbott, M.E., Influence of dihedral angles on the seismic velocities in partially molten rocks, *Earth and Planetary Science Letters 299, pp 23-32,* 2010.

Hiraga, T., Nishikawa, O., Nagase, T., and Akizuki, M., Morphology of intergranular pores and wetting angles in pelitic schists studied by transmission electron microscopy, *Contrib Mineral Petrol 141, pp 613-622,* 2001.

Hirth, G., and Kohlstedt, D.L., Experimental constraints on the dynamics of the partially molten upper mantle: deformation in the diffusion in the diffusion creep regime, *Journal of Geophysical Research, Vol. 100, No. B2, pp 1981-2001, 1*995.

de Hoff, R.T., Estimation of dihedral angles from stereological counting measurements*, Metallography 19, pp 209-217,* 1986.

Holness, M.B., Cheadle, M.J., and McKenzie, D., On the use of changes in dihedral angle to decode late-stage textural evolution in cumulates, *Journal of Petrology, Vol. 46, No. 8, pp 1565-1583,* 2005.
Holness, M.B., Melt-solid dihedral angles of common minerals in natural rocks, *Journal of Petrology, Vol. 47, No. 4, pp 791-800,* 2006.

Holness, M.B., Humphreys, M.C.S., Sides, R., Helz, R.T., and Tegner, C., Toward an understanding of disequilibrium dihedral angles in mafic rocks, *Journal of Geophysical Research, Vol. 17, B06207,* 2012.

Jurewicz & Jurewicz; Distribution of apparent angles on random sections with emphasis on dihedral angle measurements; *Journal of Geophysical Research, Vol. 91, Issue B9, pp 9277-9282,* 1986.

de Kloe, R., Drury, M.R., and van Roermund, H.L.M., Evidence for stable grain boundary melt films in experimentally deformed olivine-orthopyroxene rocks, *Phys Chem Minerals 27, pp 490-494,* 2000.

Kremer, J.R., Mastronarde, D.N., and McIntosh, J.R., Computer visualization of three-dimensional image data using IMOD, *Journal of Structural Biology, Vol. 116, Issue 1, pp 71-76,* 1996.

McDonough, W.F., and Sun, S.-s.,The composition of the Earth, *Chemical Geology, Vol. 120, Issues 3-4, pp 223-253,* 1995.

Philpotts, A.R., and Ague, J.J., principles of igneous and metamorphic petrology, second edition, *Cambridge University Press, pp 209,* 2009.

Reid, J.C., Comparison chart for estimating volume percentages of constituents in rocks and concentrates in the range of 1.0 to 0.1 volume percent, *American Mineralogist, Vol. 70, pp 1318-1319,* 1985.

Schmeling, H., Numerical models on the influence of partial melt on elastic, anelastic and electric properties of rocks. Part I: elasticity and anelasticity*, Physics of the Earth and Planetary Interiors Vol. 41, pp 34-57,* 1985.

Smith, C.S., Some elementary principles of polycrystalline microstructure, *International Materials Reviews, Vol. 9, No. 1, pp 1-48,* 1964.

Toramaru, A., and Fujii, N., Connectivity of melt phase in a partially molten peridotite, *Journal of Geophysical Research, Vol. 91, Issue B9, pp 9239-9252,* 1986.

Uchich, M.D., Groeber, M.A., Dimiduk, D.M., and Simmons, J.P., 3D microstructural characterization of nickel superalloys via serial-sectioning using a dual beam FIB-SEM*, Scripta Materialia, Vol. 55, pp 23-28,* 2006.

Volkert, C.A., Minor, A.M., Focused ion beam microscopy and micromachining, *MRS Bulletin, Vol. 32,* 2007.

Waff, H.S., and Faul, U.H., Effects of crystalline anisotropy on fluid distribution in ultramafic partial melts, *Journal of Geophysical Research, Vol. 97, No. B6, pp 9003-9014,* 1992.

van der Wal, D., Deformation processes in mantle peridotites, *Mededelingen van de Faculteit Aardwetenschappen der Rijksuniversiteit te Utrecht,* 1993.

van der Wal, W., Barnhoorn, A., Stocchi, P., Gradmann, S., Wu, P., Drury M., and Vermeersen, B., Glacial isostatic adjustment model with composite 3-D Earth rheology for Fennoscandia, *Geophys. J. Int., Vol. 194, pp61-77*, 2013.

Wark, D.A., Williams, C.A., Watson, E.B., and Price, J.D., Reassessment of pore shapes in microstructurally equilibrated rocks, with implications for permeability of the upper mantle, *Journal of Geophysical Research, Vol. 108, Issue B1,* 2003.

de Winter, D.A.M., Scneijdenberg, C.T.W.M., Lebbink, M.N., Lich, B., Verkleij, A.J., Drury, M.R., and Humbel, B.M., Tomography of insulating biological and geological materials using focused ion beam (FIB) sectioning and low-kV BSE imaging*, Journal of Microscopy, Vol. 233, Pt. 3, pp 372-383,* 2008.

Yoshino, T., Takei, Y., Wark, D.A., Watson, E.B., Grain boundary wetness of texturally equilibrated rocks, with implications for seismic properties of the upper mantle*, Journal of Geophysical Research, Vol. 110, B08205,* 2005.

Yoshino, T., Price, J.D., Wark, D.A., Watson, E.B., Effect of faceting on pore geometry in texturally equilibrated rocks: implications for low permeability at low porosity*, Contrib Mineral Petrol 152, pp 169-186,* 2006.

Yoshino, T., Yamazaki, D., Mibe, K., Well-wetted olivine grain boundaries in partially molten peridotite in the asthenosphere, *Earth and Planetary Science Letters 283, pp 167,173,* 2009.

Appendix A

Sample name	*Alternative name*	*Melt content (%)*	*Sinter time (min)*	*Final grain size (µm)*
F1	Fo9	10%	180	25,7
E1	Fo8	5%	180	ND[a]
A3	Fo20	3,5%	240	39,5
G1	F011	2,5%	240	ND[a]

Table 1. [a] ND is not determined

The software requires an input in the form of at least six coordinates; three for each grain. These coordinates are chosen along the solid-liquid interface of each grain. The emplacement of the x-axis and the y-axis relative to the position of the chosen points in the system is irrelevant as only the position of the points relative to one another is of importance.

The three coordinates chosen for each grain are used to calculate the centre coordinates and the radius of each grain by use of the following steps:

Chord $(x,y)_1 – (x,y)_2$ is described by the general equation,

$$y = ax + b \tag{1.1}$$

where

$$a = \frac{\Delta y}{\Delta x} = \frac{(y_2 - y_1)}{(x_2 - x_1)} \tag{1.2}$$

$$y_1 = \frac{(y_2 - y_1)}{(x_2 - x_1)} x_1 + b \tag{1.3}$$

Solving equation (1.3) for *b* results in the total equation for the chord between the first two sets of chosen coordinates. This step is repeated for the chord running between the second and the third set of coordinates.

The line running through the middle of a chord between coordinates on the rim of a circle, in the direction normal to the chord also runs through the centre of the circle. This is shown in fig.2.

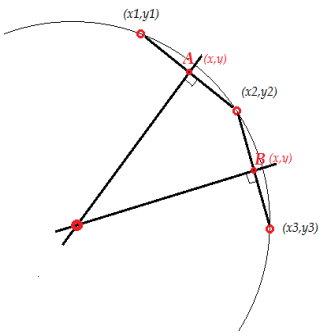

Figure 2.

The normals of the chord are lines with the same general equation (1.1). The coefficient of this line can be expressed in terms of the coefficient of the chord line. Here we make use of the fact that the product of the coefficients of two lines that are perpendicular to each other equals -1 (Figure 3).

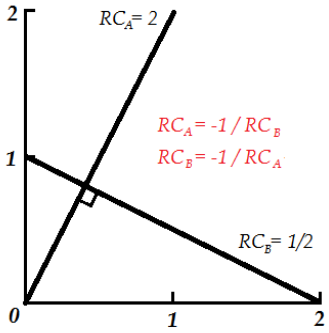

Figure 3.

The equation for the normal to the a chord connecting (x_1, y_1) and (x_2, y_2) is then

$$\left(\frac{y_1+y_2}{2}\right)=\frac{-1}{\left(\frac{y_2-y_1}{x_2-x_1}\right)}\cdot\left(\frac{x_1+x_2}{2}\right)+b \qquad (2.1)$$

This is repeated for the line normal to the second chord. Because both lines run through the centre of the circle, the intersection point of the two lines calculated in step 2 then represents the centre point of the circle attributed to the coordinates of the first grain.

The radius of the circle is found using Pythagoras equation in which the coordinates of the centre and any one of the points on the rim of the circle are used. The two short sides of the triangle through

these points are represented by the increase of x and y, and the long side of the triangle represents the radius of the circle (equation 3.1).

$$r = \sqrt{(x_1 - x_{centre})^2 + (y_1 - y_{centre})^2} \tag{3.1}$$

Now the centre and radius of the first grain is determined, these steps are repeated for the other three coordinates to obtain the centre and radius of the other grain.

Choosing the x-axis such that both circle centers can be plotted along the x-axis and the first circle being at coordinates (0,0) the x-coordinate of the second circle is determined by the distance between the two circles in their original positions, while the y-coordinate is set to zero. The x-coordinate of the centre of the second circle is then calculated with equation (4.1).

$$x_{centre2}^{new} = \sqrt{(x_{centre2} - x_{centre1})^2 + (y_{centre2} - y_{centre1})^2} \tag{4.1}$$

The intersection points of the two circles represent the point at which the solid-liquid interface at the grain boundaries change into a solid-solid interface, and therefore the point in which the dihedral angle between the two grains should be measured. The point of intersection is determined using the length of the chords connecting the two intersection points. Because one circle has its centre in the origin and the other has its centre on the x-axis at a given x-coordinate *a*, the equations representing the two circles are (5.1) and (5.2).

$$x^2 + y^2 = r_1^2 \tag{5.1}$$

$$(x-a)^2 + y^2 = r_2^2 \tag{5.2}$$

Solving for y in equation (5.1) and incorporating in equation (5.2) results in equation (5.3) and (5.4).

$$y^2 = r_1^2 - x^2 \tag{5.3}$$

$$(x-a)^2+(r_1^2-x^2)=r_2^2 \tag{5.4}$$

Solving equation (5.4) for x results in equation (5.5.1).

$$-2xa+a^2=r_2^2-r_1^2 \tag{5.5.1}$$

This can be rewritten as equation (5.5.2).

$$x=\frac{a^2-r_2^2+r_1^2}{2a} \tag{5.5.2}$$

Incorporating x back in equation (5.3), solving for *y,* and rewriting the equation through equations (5.6.1) to (5.6.3), yields equation (5.6.4).

$$y^2=r_1^2-x^2=r_1^2-\left(\frac{a^2-r_2^2+r_1^2}{2a}\right)^2 \tag{5.6.1}$$

$$y^2=\frac{4a^2r_1^2-(a^2-r_2^2+r_1^2)^2}{4a^2} \tag{5.6.2}$$

$$y=\sqrt{\frac{4a^2r_1^2-(a^2-r_2^2+r_1^2)^2}{4a^2}} \tag{5.6.3}$$

$$y=\frac{1}{2a}\cdot\sqrt{4a^2r_1^2-(a^2-r_2^2+r_1^2)^2} \tag{5.6.4}$$

The value for y is half of the total length of the chord connecting the intersection points, but since the centers of the circles are on the x-axis, half the chord will be below this axis and half of it will be above the axis. The value obtained for *y* therefore represents the y-coordinate of the intersection point. The x-coordinate of the intersection point is then again calculated using Pythagoras. (5.7).

$$x=\sqrt{r_1^2-y^2} \tag{5.7}$$

To calculate the dihedral angle, the tangents of both circles in the intersection are required. These tangents are described by the lines perpendicular to the lines connecting the centers of the circles to the intersection point. The equation describing the lines between the center of the circle and the intersection point for circle 1 and circle 2 are given in equations (6.1.1) and (6.1.2) respectively

$$y = \frac{\Delta y}{\Delta x} = \left(\frac{y_{intersection} - y_{centre1}}{x_{intersection} - x_{centre1}} \right) \cdot x \tag{6.1.1}$$

$$y = \frac{\Delta y}{\Delta x} = \left(\frac{y_{intersection} - y_{centre2}}{x_{centre2} - x_{intersection}} \right) \cdot x \tag{6.1.2}$$

In order to obtain the tangents of the circle in the intersection points, the normals of the lines described by equations 6.1.1 and 6.1.2 are calculated using the conversion shown in fig.2. The equations describing the tangents then become equations (6.2.1) and (6.2.2) respectively.

$$y = \frac{-1}{\left(\frac{y_{intersection} - y_{centre1}}{x_{intersection} - x_{centre1}} \right)} \cdot x \tag{6.2.1}$$

$$y = \frac{-1}{\left(\frac{y_{intersection} - y_{centre2}}{x_{centre2} - x_{intersection}} \right)} \cdot x \tag{6.2.2}$$

The dihedral angle, represented by the angle between the tangents of the two circles, is calculated using the x-axis as a reference. The angles between the tangents and the x-axis are described in equations (6.3.1) and (6.3.2) being the inverse tangent of the slope of the circle in the intersection point. Because the equations should describe the angle between the tangent line and the x-axis, the sign of the slope is irrelevant. Therefore, the absolute value is used.

$$\alpha_1 = \left| \tan^{-1} \left(\frac{-1}{\left(\frac{y_{intersection} - y_{centre1}}{x_{intersection} - x_{centre1}} \right)} \right) \right| \qquad (6.3.1)$$

$$\alpha_2 = \left| \tan^{-1} \left(\frac{-1}{\left(\frac{y_{intersection} - y_{centre2}}{x_{centre2} - x_{intersection}} \right)} \right) \right| \qquad (6.3.2)$$

The dihedral angle is then determined by taking a 180° angle and subtracting α_1 and α_2 (fig.4).

$$\Theta = 180 - (\alpha_1 + \alpha_2) \qquad (7.1)$$

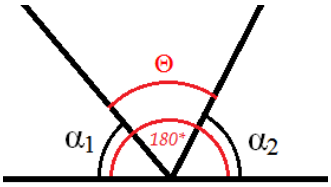

Figure 4.

In case of a dihedral angle that describes the angle between a grain boundary with fully developed facets and a grain boundary with a more circular character, the dihedral can be represented by the angle between a circle and a straight line.

To determine this angle, an equation has to be developed for describing the circular grain boundary and a separate equation describing the faceted grain boundary which will be a line.

Straight and curved grain boundary

Equations for line and circle are needed (1 and 2);

$$lijn \rightarrow y = \left(\frac{y_2 - y_1}{x_2 - x_1} \right) \cdot x + y_1 - \left(\frac{y_2 - y_1}{x_2 - x_1} \right) \cdot x_1 \tag{1}$$

$$cirlce \rightarrow 0 = (x - x_c)^2 + (y - y_c)^2 - \left((x_1 - x_c)^2 + (y_1 - y_c)^2 \right) \tag{2}$$

Equate the equations and determine a, b and c in the ABC-formula;

$$a = x^2 \cdot \left(\left(\frac{y_2 - y_1}{x_2 - x_1} \right)^2 + 1 \right) \tag{3}$$

$$b = x \cdot \left(\left(2 \cdot \left(- \left(\frac{y_2 - y_1}{x_2 - x_1} \right) \cdot x_1 - y_c + y_1 \right) \cdot \left(\frac{y_2 - y_1}{x_2 - x_1} \right) \right) - 2x_c \right) \tag{4}$$

$$c = r^2 = (x_1 - x_c)^2 + (y_1 - y_c)^2 \tag{5}$$

The determinant becomes;

$$D = \left(x \cdot \left(\left(2 \cdot \left(- \left(\frac{y_2 - y_1}{x_2 - x_1} \right) \cdot x_1 - y_c + y_1 \right) \cdot \left(\frac{y_2 - y_1}{x_2 - x_1} \right) \right) - 2x_c \right) \right)^2 - \left(4 \cdot x^2 \cdot \left(\left(\frac{y_2 - y_1}{x_2 - x_1} \right)^2 + 1 \right) \cdot (x_1 - x_c)^2 + (y_1 - y_c)^2 \right) \tag{6}$$

Solutions are given by the following equation (7);

$$x = \frac{-b \pm \sqrt{D}}{2a} \tag{7}$$

The obtained x-values should be implemented in either one of the original equations to obtain the corresponding y-values. Then use the known circle and the intersection points to determine the angle between the straight line and the tangent of the circle in the point of intersection.

Appendix B

Samples:

F1 (10% melt)

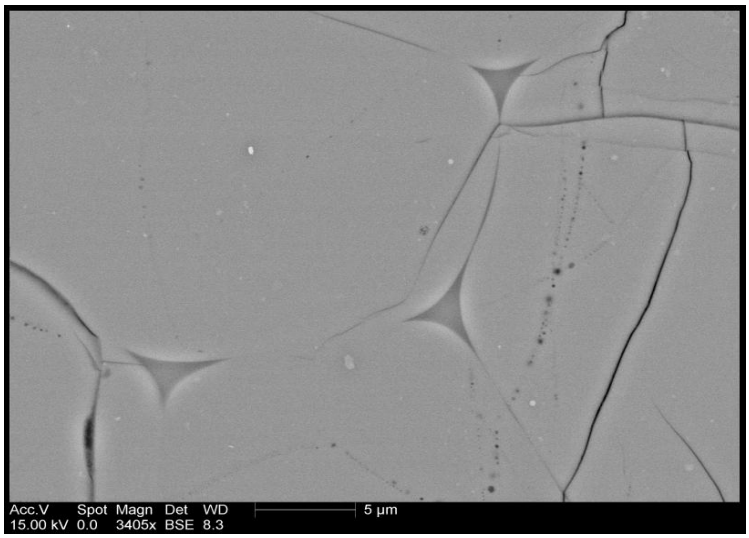

All dihedral angles measured

angle name	average	std. dev.
F1A004-1	9,1	1,7
F1A006-1	6,4	1,6
F1A006b-1	7,9	0,4
F1A013a-1	7,4	1,4
F1A013b-1	4,3	3,5
F1A009-1	6	1,4
F1A011-1	5,4	2
F1A016a-1	10,8	2,5
F1A016a-6	5,5	1,9
F1A016a-11	6,7	2
F1-001-01	6	0,9
F1-001b-01	0,2	0,1
F1-001c-01	7,5	1,9
F1-001d-01	15,3	2,6
F1-001e-01	1,6	1,3
F1-001f-01	0	0
F1-001g-01	0	0
F1-002-01	17,2	3,7
F1-002b-01	9,1	1,5
F1-002c-01	3,8	4,2
F1-003-01	4,6	1,8
F1-003b-01	3,9	3,4
F1-003c-01	4,1	0,8
F1-003d-01	0	0
F1-004-01	9,4	3,8
F1-004b-01	7,9	3,7
F1-004c-01	12,2	1,6

angle name	average	std. dev.
F1-004d-01	7,7	2
F1-004e-01	0	0
F1-005-01	8,2	4,6
F1-005b-01	5,7	1,4
F1-005c-01	0	0
F1-006-01	7	1,7
F1-006b-01	0	0
F1-006c-01	0	0
F1-007-01	1	1,6
F1-007b-01	3,4	1,9
F1-007c-01	10,9	1,4
F1-007d-01	12,3	4,4
F1-007e-01	21,7	2,3
F1-007f-01	3,6	1,8
F1-007g-01	8,2	2,3
F1-008-01	14,2	1,5
F1-008b-01	9,1	3,5
F1-008c-01	0	0
F1-008d-01	8,7	1
F1-008e-01	3,9	0,8
F1-010-01	7,4	1,3
F1-010b-01	5,5	1,8
F1-010c-01	0	0
F1-010d-01	8,1	0,9
F1-010e-01	16,1	3,2
F1-010f-01	9.6	0.2

E1 (5% melt)

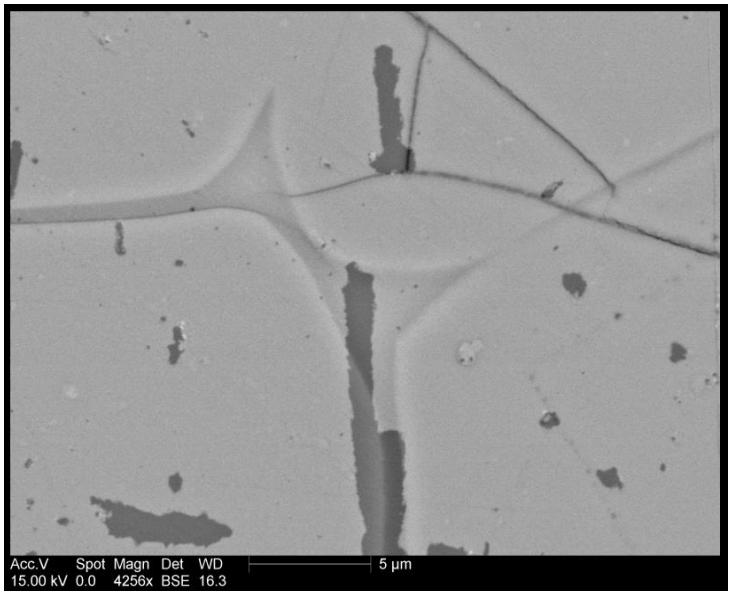

All dihedral angles measured

angle name	*mean*	*std. dev.*
E1-005-1	26,2	2,4
E1-005-5	13,3	0,2
E1-005b-1	0	0
E1-007-1	18,3	2,3
E1-007b-1	0	0
E1-007c-1	0	0
E1-008-1	22,9	4,1
E1-008b-1	0	0
E1-008c-1	0	0
E1-011-01	4,4	0,8
E1-013-01	7,3	0,5
E1-014-01	0	0
E1-014b-01	0	0
E1-014c-01	0	0
E1-015-01	73,3	73,3
E1-015b-01	45,1	45,1
E1-015c-01	54,2	54,2
E1-016-01	7,9	0,4
E1-016b-01	54,7	0,5
E1-019-01	0	0
E1-019b-01	0	0
E1-019c-01	0	0
E1-019d-01	0	0
E1-019e-01	0	0
E1-022-01	0	0
E1-022b-01	0	0
E1-023-01	4,5	3,3
E1-026-01	3,4	1,4

A3 (3,5% melt)

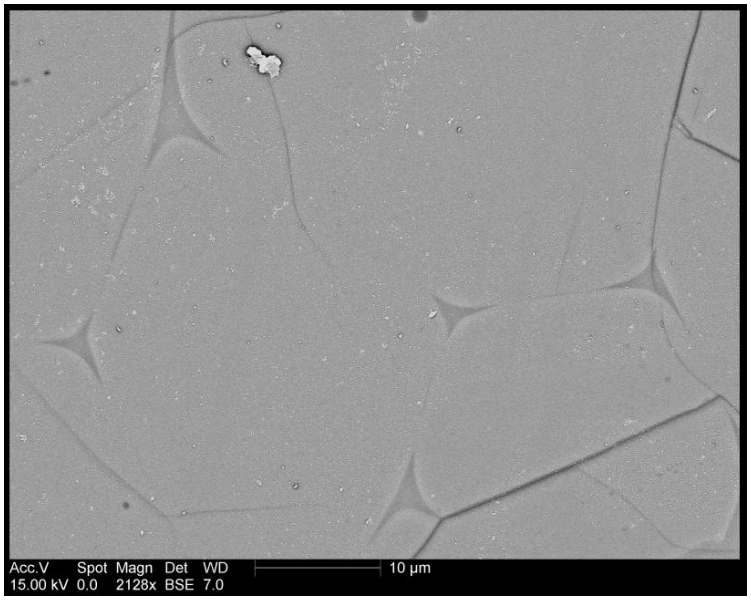

All dihedral angles measured

angle name	*mean*	*std. dev.*
A3-002-01	16,8	3,1
A3-002b-01	37,9	3,2
A3-002c-01	0	0
A3-002d-01	0	0
A3-002e-01	0	0
A3-002f-01	0	0
A3-003-01	14,4	1,1
A3-003b-01	0	0
A3-003c-01	0	0
A3-003d-01	0	0
A3-004-01	9,8	2
A3-004b-01	0	0
A3-004c-01	0	0
A3-005-01	8,9	2,4
A3-005b-01	11,5	3,4
A3-005c-01	0	0
A3-005d-01	0	0
A3-006-01	9,3	2,3
A3-006b-01	7,4	1,1
A3-006c-01	0	0
A3-007-01	8,8	1,3
A3-007b-01	14,1	1
A3-007c-01	5,5	1,3
A3-007d-01	3,2	2,5

angle name	*mean*	*std. dev.*
A3-007e-01	2,7	1,1
A3-007f-01	0	0
A3-007g-01	0	0
A3-008-01	12,7	2,1
A3-008b-01	14,9	4,8
A3-008c-01	9,5	1,4
A3-008d-01	8,4	2,1
A3-008e-01	0	0
A3-009-01	11,9	4,2
A3-009b-01	12,4	1,9
A3-009c-01	7,6	3,9
A3-009d-01	4,4	3,5
A3-009e-01	29,9	4,9
A3-009f-01	4,6	2,9
A3-009g-01	15,6	1,4
A3-009h-01	0	0
A3-010-02	14	0,8
A3-010b-01	0	0
A3-011-01	4	1,8
A3-011b-01	0	0
A3-011c-01	0	0
A3-012-01	1,9	1,5
A3-012b-01	0	0

G1 (2,5% melt)

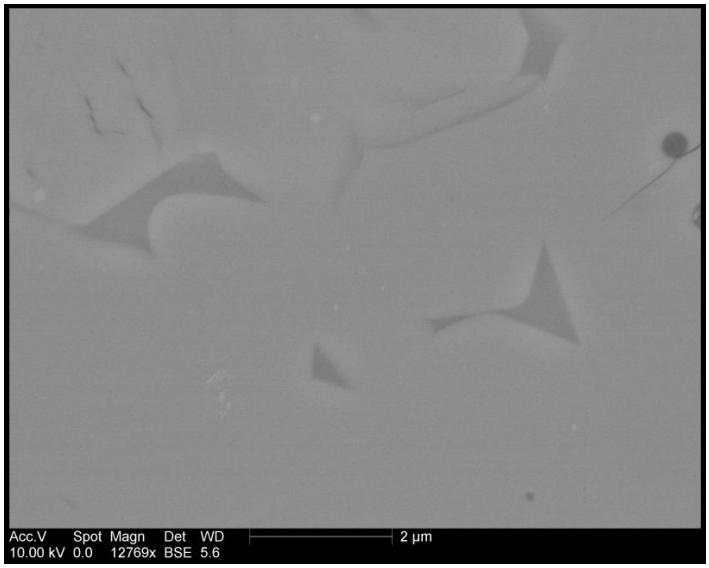

All dihedral angles measured

angle name	*mean*	*std. dev.*
G1-001-01	45,8	1,9
G1-001b-01	66,8	1,5
G1-001c-01	118,6	4,8
G1-001d-01	136,4	1,5
G1-007-01	23,4	1,9
G1-007b-01	6,3	0,9
G1-007c-01	78,2	3,1
G1-008-01	68,3	5,1
G1-009-01	10	1,6
G1-009b-01	16,2	5,6
G1-009c-01	80,2	1,3
G1-009d-01	16,6	3
G1-009e-01	101,9	1,7
G1-011-01	24,8	6,7
G1-011b-01	51,8	4,5
G1-012-01	21,8	3
G1-013-01	18,8	5,3
G1-013b-01	23	2,3
G1-013c-01	17,3	4
G1-013d-01	16,3	2
G1-014-01	48,2	4,5
G1-014b-01	28,3	4,4
G1-014c-01	21,5	4,6
G1-015-01	31,4	6,3
G1-015b-01	28,4	3,8
G1-015c-01	62,4	3,7
G1-015d-01	0	0
G1-018-01	24	2,2
G1-021-001	23,4	1,7
G1-021b-001	26,4	8,7
G1-021c-001	46,8	2,1

angle name	*mean*	*std. dev.*
G1-021d-01	0	0
G1-021e-01	0	0
G1-022-001	27,3	1,3
G1-022b-001	28,6	2,3
G1-022c-001	68,2	7,4
G1-023-001	22,7	6
G1-023b-001	28,3	1,3
G1-023c-001	66,3	4,1
G1-024-001	50,2	4,5
G1-024b-001	60,4	3,6
G1-024c-001	18,9	3,9
G1-024d-001	49,9	5,8
G1-024e-001	83,1	2,9
G1-026-001	18,5	3,4
G1-026b-001	16,5	6
G1-026c-001	12,1	3,1
G1-026d-001	78	1,2
G1-027-001	37,7	5,2
G1-027b-001	10,8	2,4
G1-028-001	72,3	6
G1-028b-001	54,5	0,6
G1-028c-001	20	1,6
G1-028d-001	21,4	3,3
G1-029-001	71,7	4
G1-029b-001	84,6	8,9
G1-029c-001	51,8	2,6
G1-029d-001	26,7	2,7
G1-029e-001	20,8	1,4
G1-029f-001	42,7	1,5
G1-029g-001	44,6	4,5